

PHOTOPRODUCTION OFF NUCLEI

Part II: Particle and Jet Production

S. Roesler*

Universität Siegen, Fachbereich Physik, D-57068 Siegen, Germany

R. Engel†

*Universität Leipzig, Fachbereich Physik, D-04109 Leipzig, Germany
and Universität Siegen, Fachbereich Physik, D-57068 Siegen, Germany*

and

J. Ranft‡

*Departamento de Física de Partículas, Universidade de Santiago de Compostela,
E-15706 Santiago de Compostela, Spain*

Abstract

High energy multiparticle photoproduction off nuclear targets is studied. The photon is assumed to interact in direct scattering processes or as a resolved $q\bar{q}$ -state according to the Generalized Vector Dominance Model. In the description of resolved interactions multiple soft and hard processes in each $q\bar{q}$ -nucleon interaction are taken into consideration. The model, formulated within the framework of the two-component Dual Parton Model, is shown to agree with hadron production data from real and weakly virtual photon-nucleus interactions. Differences between multiparticle production in photon-nucleus and hadron-nucleus interactions and features of jet production in photon-nucleus collisions at HERA-energies are discussed.

Siegen SI 96-14
Santiago de Compostela US-FT/45-96
revised version, November 1997

*present address: CERN, CH-1211 Genève 23, Switzerland

†present address: University of Delaware, Bartol Research Institute, Sharp Lab., Newark, DE 19716, U.S.A.

‡present address: Universität Siegen, Fachbereich Physik, D-57068 Siegen, Germany

1 Introduction

Many features of high energy photoproduction off hadrons are well understood within the QCD-improved parton model: the photon may couple directly to a parton of the hadron (*direct* processes) or it may enter the scattering process as a hadronic fluctuation (*resolved* processes) (recent reviews are given in [1, 2]). Since the lifetimes of these hadronic fluctuations are typically long enough to develop properties of ordinary hadrons they can interact in soft and hard resolved processes [3, 4]. The classification into direct and resolved photon interactions has been confirmed by many experiments [5, 6, 7]. Moreover, it has been shown that both classes of processes exhibit different properties concerning multiparticle production [3, 4, 5, 8, 9]. Here, we extend a previous study of photon–nucleus cross sections and their high energy shadowing behavior [10] to particle production. This is done by applying the two-component Dual Parton Model (DPM) [11, 12, 13, 14, 15] to photoproduction off nuclei.

The two-component DPM is based on the DPM describing soft particle production (for a review see [16]) and treats high- p_{\perp} processes using lowest order perturbative QCD. This model has been proven to be very reliable in describing the main features of hadron–hadron [12, 13], photon–hadron [14, 15], photon–photon [15], hadron–nucleus [17], and nucleus–nucleus collisions [17]. Here, the two-component DPM is applied to photon–nucleus collisions for the first time. The two channels which are of particular importance as a basis for our present study are hadron–nucleus and photon–hadron collisions.

In hadron–nucleus collisions the multiple interaction process of the hadron with target nucleons which explains the “shadowing”-effect, is understood in the framework of the Gribov–Glauber approximation [18, 19, 20]. The two-component DPM incorporates the Gribov–Glauber approximation and treats each hadron–nucleon interaction by pomeron and reggeon exchanges. DTUNUC 2.0, a Monte Carlo (MC) realization of the two-component DPM for hadron–nucleus and nucleus–nucleus collisions, includes the Glauber-formalism [21], the PHOJET model [14, 15] for each hadron–nucleon or nucleon–nucleon collision, a formation zone intranuclear cascade model, and models for spectator deexcitation and disintegration [22, 23]. As it will be shown further below, results on particle production in hadron–nucleus collisions obtained with DTUNUC 2.0 are in good agreement with data.

The description of photon–hadron interactions within the two-component DPM takes the above mentioned dual nature of the photon into consideration. In analogy to hadron–hadron interactions, the resolved photon interactions are described in terms of multiple soft and hard pomeron and soft reggeon exchanges. Parton jet and minijet production in resolved processes as well as direct processes are calculated in lowest order perturbative QCD. The MC realization PHOJET has been compared in several applications to photoproduction data from the HERA collider and a reasonable agreement was found [8, 24, 25].

Using all informations from hadron–nucleus and photon–hadron collisions it can be expected that the two-component DPM also gives a reasonable description of multiparticle photoproduction off nuclei up to very high energies. Such a model might be useful for the study of general properties of photon–nucleus interactions as well as for the calculation of theoretical predictions (for example at HERA energies), cosmic ray cascade simulations, or shielding problems at TeV-lepton colliders.

In Sect. 2 we summarize the basic ideas of the description of hadron–nucleon and photon–

nucleon interactions within the two-component DPM. Furthermore, its application to photon–nucleus interactions is presented. In Sect. 3 we demonstrate that the model is able to describe characteristic features of measured particle production in photon–nucleus interactions. The nuclear dependence of multiparticle photoproduction off nuclei and direct as well as resolved jet production are studied. Predictions for HERA-energies are given. Finally, in Sect. 4 we summarize our results.

2 The two-component Dual Parton Model

2.1 Photon–nucleon interactions

In the following, we give a summary of the basic ideas of the two-component DPM with emphasis to the description of photon–nucleon interactions as implemented in the MC generator PHOJET. More detailed discussions can be found in Refs. [14, 15].

The physical photon state is approximated as a superposition of a bare photon and of virtual hadronic states having the same quantum numbers as the photon. The bare photon may interact in direct processes. This direct contribution is estimated by lowest order perturbative QCD. The interactions of the hadronic fluctuations of the photon are called resolved processes and are described within the framework of the two-component DPM in terms of reggeon and pomeron exchanges. We distinguish soft and hard resolved processes according to the transverse momenta of the intermediate states of the pomeron exchange graph: By definition, scattering processes resulting in at least one parton having a transverse momentum larger than a cutoff momentum $p_{\perp}^{\text{cutoff}} = 3 \text{ GeV}/c$ are called hard interactions. All other processes are classified as soft interactions.

The amplitude describing the scattering of the hadronic fluctuation V with a nucleon N is parametrized using a two-channel eikonal formalism [14, 13]. In impact parameter representation, the amplitude reads [14]

$$a_{VN}(s, b) = \frac{i}{2} \left(1 - e^{-\chi(s, b)} \right), \quad (1)$$

with the eikonal function

$$\chi(s, b) = \chi_S(s, b) + \chi_H(s, b) + \chi_D(s, b) + \chi_C(s, b). \quad (2)$$

Here, the χ_i 's denote the contributions from the different Born graph amplitudes: soft pomeron and reggeon (S), hard pomeron (H), triple- and loop-pomeron (D), and double-pomeron amplitudes (C). The Born graph amplitudes of the soft processes are calculated using Gribov's reggeon field theory [26, 19]. Assuming universality of soft interactions, the free parameters of the model (pomeron couplings, pomeron intercept, triple-pomeron coupling, and slope parameters) have been determined by a global fit to pp , $p\bar{p}$, and γp cross section and slope data [14]. However this universality cannot be applied to photon interactions involving large transverse momenta. Lowest order perturbative QCD is used to calculate the resolved and direct hard photon cross sections [14, 27].

The optical theorem relates the total cross section (i.e. elastic scattering, diffraction dissociation, and nondiffractive inelastic scattering) to the discontinuity of the amplitude (1) taken at vanishing momentum transfer. At high energies, the discontinuity can be expressed as a sum over terms which correspond to graphs with a certain number of cut pomerons (Abramovski–Gribov–Kancheli cutting rules [28]). Therefore, one obtains for the exclusive cross section for k_c cut soft pomerons, l_c cut hard pomerons, m_c cut triple- and loop-pomeron graphs, and n_c cut double-pomeron graphs

$$\sigma(k_c, l_c, m_c, n_c, s, b) = \frac{(2\chi_S)^{k_c}}{k_c!} \frac{(2\chi_H)^{l_c}}{l_c!} \frac{(2\chi_D)^{m_c}}{m_c!} \frac{(2\chi_C)^{n_c}}{n_c!} e^{-2\chi(s,b)} \quad (3)$$

with

$$\int d^2b \sum_{k_c+l_c+m_c+n_c=1}^{\infty} \sigma(k_c, l_c, m_c, n_c, s, b) = \sigma_{VN}^{\text{tot}} - \sigma_{VN}^{\text{el}}. \quad (4)$$

Both resolved soft and hard interactions are unitarized, i.e. a single $q\bar{q}$ -nucleon scattering may be built up of several soft and hard interactions. In contrast to resolved processes, absorptive corrections to direct photon interactions are suppressed by one order of the fine structure constant α_{em} and are therefore neglected.

In order to relate the cross sections given in Eq.(3) to final state parton configurations, we use the equivalence between the reggeon and pomeron exchange amplitudes and certain color flow topologies [29]. In Fig. 1 the color flows of single reggeon (a) and single pomeron exchange processes (c) are shown together with the corresponding cuts. Whereas a cut reggeon yields one color-field chain (string) (Fig. 1b), a cut pomeron results in two strings (Fig. 1d) which are assumed to fragment independently into hadrons. In the large N_c limit of QCD (with N_c being the number of colors) the same color flow picture of the pomeron is also found in hard interactions.

For pomeron cuts involving a hard scattering, the parton kinematics as well as the flavors and colors are sampled according to the QCD-improved Parton Model using leading-order matrix elements. We use the GRV parametrizations of the parton distribution functions (PDF) of the photon [30] and the nucleon [31]. Both, initial and final state parton showers are treated. For the latter the Monte Carlo (MC) realization as implemented in JETSET [32, 33] is applied.

In case of pomeron cuts without large momentum transfer, we assume the partonic interpretation of the DPM: hadronic fluctuations of the photon are split into a quark-antiquark pair whereas baryons are approximated by a quark-diquark pair. The longitudinal momentum fractions of the partons are given by Regge asymptotics [34, 35, 36, 37]. The valence quark momentum fraction x inside a nucleon is sampled according to $\rho(x) \sim (1-x)^{1.5}/\sqrt{x}$ whereas the momentum fraction of a valence quark inside a hadronic fluctuation of a photon is obtained from $\rho(x) \sim 1/\sqrt{x(1-x)}$. For multiple interaction events, the sea quark momenta are sampled using a $\rho(x) \sim 1/x$ behavior. The transverse momenta of the soft partons are not predicted by the DPM. Here, we assume an exponential distribution $d^2N_s/dp_{\perp}^2 \sim \exp(-\beta p_{\perp})$. The energy-dependent slope parameter β is obtained requiring a smooth transition between the transverse momentum distributions of the soft constituents and the hard scattered partons.

For single diffractive and central diffractive processes, the parton configurations are generated using the ideas described above applied to pomeron-photon/hadron/pomeron scattering

processes [38]. Hence, a diffractive triple-pomeron or loop-pomeron cut can also involve hard scattering subprocesses resulting in a rapidity gap event with jets.

All strings are hadronized using JETSET 7.3 [32, 33].

Finally it should be mentioned that the model is limited to photon virtualities $Q^2 \ll s$ with $Q^2 < 9 \text{ GeV}^2$ [15].

2.2 The event generator DTUNUC 2.0 for photon–nucleus collisions

The MC event generator DTUNUC 2.0 for hadron–, photon–, and nucleus–nucleus collisions is based on its previous version [39, 40] incorporating the following new features:

- DTUNUC is extended to the description of photoproduction off nuclei.
- Particle production in each photon–, hadron–, and nucleon–nucleon interaction is based on the MC realization PHOJET [14, 15] of the two-component DPM which includes multiple soft and hard pomeron exchanges and diffraction.
- A formation zone intranuclear cascade is treated in both, the projectile and target spectators including evaporation of nucleons and light nuclei from excited spectators, spectator deexcitation via photon emission, and fragmentation of light spectator nuclei [22, 23].

The generation of a photon–nucleus⁴ particle production event proceeds as follows: The treatment of any interaction starts with sampling of an initial spatial configuration according to nuclear densities and of the Fermi-momenta of the nucleons. The number of nucleons involved in the scattering process with the photon is obtained according to the Glauber approximation. We use the MC algorithm of [21], here extended to photon projectiles. The inelastic cross section for the scattering of a photon with virtuality Q^2 with a nucleus A at a squared photon–nucleon c.m. energy s and at impact parameter b reads [10]

$$\sigma_{\gamma A}(s, Q^2, b) = 4\pi\alpha_{\text{em}} \int_{M_0^2}^{M_1^2} dM^2 D(M^2) \left(\frac{M^2}{M^2 + Q^2} \right)^2 \left(1 + \epsilon \frac{Q^2}{M^2} \right) \sigma_{VA}(s, Q^2, M^2, b) \quad (5)$$

$$\sigma_{VA}(s, Q^2, M^2, b) = \int \prod_{j=1}^A d^3r_j \rho_A(\vec{r}_j) \left(1 - \left| \prod_{i=1}^A [1 - \Gamma(s, Q^2, M^2, \vec{b}_i)] \right|^2 \right). \quad (6)$$

Corresponding to the assumptions of the Generalized Vector Dominance Model (GVDM) (see for example [3, 41] and references therein) we integrate in (5) over the masses M of the hadronic fluctuations of the photon. $D(M^2)$ denotes the density of hadronic states per unit mass-squared interval. ϵ is the ratio between the fluxes of longitudinally and transversally polarized photons. Eq.(6) relates the inelastic cross section σ_{VA} for the interaction of the

⁴Here, we restrict our discussion to photon projectiles. The treatment of hadron–nucleus collisions is similar; the discussion of nucleus–nucleus collisions is not within the scope of this paper

hadronic fluctuation with the nucleus to the amplitude Γ for the interaction of the hadronic fluctuation with a nucleon

$$\Gamma(s, Q^2, M^2, \vec{b}) = \frac{\sigma_{VN}(s, Q^2, M^2)}{4\pi B(s, Q^2, M^2)} (1 - i\rho) \exp\left(\frac{-\vec{b}^2}{2B(s, Q^2, M^2)}\right), \quad (7)$$

$$\sigma_{VN}(s, Q^2, M^2) = \frac{\tilde{\sigma}_{VN}(s, Q^2)}{M^2 + Q^2 + C^2}. \quad (8)$$

We refer to [10] for the calculation of the M^2 -independent quantity $\tilde{\sigma}_{VN}$, the slope B , and the parameters entering the expressions. The integration over the coordinate space in (6) is performed using one-particle Woods–Saxon density distributions ρ_A [42]. With the impact parameter b and the mass M of the hadronic fluctuation which are sampled according to Eqs.(5,6), we obtain for the probabilities p_i that an inelastic interaction between the projectile and nucleon i takes place [10, 21]

$$p_i = \Gamma(\vec{b}_i) + \Gamma^*(\vec{b}_i) - \Gamma(\vec{b}_i)\Gamma^*(\vec{b}_i). \quad (9)$$

Note that b_i is the impact parameter for the interaction of the hadronic fluctuation with the nucleon i for a fixed spatial configuration of nucleons.

As it has been discussed in Sect. 3 of Ref. [10], hadronic fluctuations with $M^2 > (2p_{\perp}^{\text{cutoff}})^2$ predominantly interact in point-like interactions⁵, i.e. in direct interactions and in interactions which are characterized by the anomalous component of the photon PDF. In both cases, the virtuality of the $q\bar{q}$ -system allows to calculate the photon– $q\bar{q}$ coupling perturbatively. We denote the corresponding cross sections with $\sigma_{\gamma N}^{\text{dir}}$ and $\sigma_{\gamma N}^{\text{ano}}$ and refer to [10] for their calculation within lowest order perturbative QCD. Here we shall again consider the extreme case that in these processes the hadronic fluctuation of the photon interacts with only one target nucleon. Therefore, in the fraction $A \cdot (\sigma_{\gamma N}^{\text{dir}} + \sigma_{\gamma N}^{\text{ano}}) / \sigma_{\gamma A}^{\text{tot}}$ of all events only one hard resolved (representing the anomalous component) or one direct photon interaction is sampled.

Furthermore, as for the calculation of cross sections [10], the coherence length of the photon is taken into consideration which effectively leads to a suppression of the Glauber-cascade at low energies. Particle production in each inelastic interaction of the photon or its hadronic fluctuation with a nucleon is treated by the MC realization PHOJET of the two-component DPM (see Sect.2.1). The photon–nucleon interactions are followed by a formation zone intranuclear cascade in the target spectator and by subsequent evaporation processes of nucleons and light nuclei as well as by spectator deexcitation, and by the fragmentation of light spectator nuclei [22, 23].

3 Particle production

For studying photoproduction off nuclei we assume the logical sequence to be as follows: As mentioned earlier soft hadronic interactions exhibit universal features irrespective of the

⁵Note that in our definition of “point-like photon interactions” [10] interactions of low-mass $q\bar{q}$ -fluctuations with only one target nucleon are not included

nature of the colliding particles. This fact was already emphasized by Engel and Ranft in [15] where the description of high energy hadron–hadron and photon–hadron interactions based on the two-component DPM was extended to photon–photon interactions. Here, we want to proceed in an analogous way. We start from the description of photon–hadron and hadron–nucleus interactions and show that the model may also provide a reasonable description of photon–nucleus interactions.

Photon–hadron collisions have been discussed in the framework of the two-component DPM elsewhere [14, 15]. Furthermore, also numerous studies of hadron–nucleus collisions within this model exist (see for instance [39, 40, 17] and references therein). Of course for the latter interaction channel it has to be verified that the new version of DTUNUC is able to describe the data. Since this has not yet been demonstrated we give a few examples further below.

Based on the reasonable description of these two interaction channels the model is then applied to multiparticle photoproduction off nuclei. This application may serve as a severe test of the model since it carries no further freedom.

3.1 Hadron–nucleus interactions

In Table 1 average shower particle multiplicities calculated for interactions of positively charged pions and protons with different target nuclei at 50, 100, and 150 GeV are given. Here, shower particles are defined as singly charged particles with Lorentz- β values exceeding 0.7. These results are compared to data taken from Ref. [43]. For all configurations there is a reasonable agreement between the calculated and measured values.

The distribution of the multiplicity of shower particles produced in interactions of 525 GeV pions in nuclear emulsions is plotted in Fig. 2a. Model results shown as histogram are compared to data [44]. As this plot demonstrates also the distribution of the shower particle multiplicity is reproduced by the model.

Calculated and measured [44] pseudorapidity distributions of shower particles are shown in Fig. 2b again for pion–emulsion interactions at 525 GeV and, additionally, for 60 GeV.

The invariant π^0 cross section as a function of the transverse momentum in proton–gold collisions at 200 GeV has been measured by the WA80-Collab. [45]. In Fig. 3 we compare our calculations to these data and find a reasonable agreement. Corresponding to the kinematic cuts of the experiment the pseudorapidity range $1.5 \leq \eta \leq 2.1$ is considered only.

3.2 Photon–nucleus interactions

3.2.1 General properties of the model

Before comparing model results to data from lepton–nucleus interactions let us first outline differences between hadron– and photon–nucleus collisions with respect to properties of the Glauber-cascade and multiplicities at fixed projectile energy. In lepton–nucleus interactions the projectile photon has varying energies and virtualities and a direct comparison with hadron–nucleus collisions would be less conclusive.

In Fig. 4 we present average numbers of target nucleons interacting with the projectile $\langle \nu_t \rangle$ and multiplicities of shower $\langle N_s \rangle$ and heavy particles $\langle N_h \rangle$ (charged particles with $\beta \leq 0.7$) calculated for pion-, real photon-, and weakly virtual photon-copper interactions at energies of the projectile in the nucleus rest system between 10 GeV and 100 TeV. Differences between the ν_t -values for pion and photon projectiles at fixed energy arise from differences between the pion-nucleon cross section and the (averaged over all masses M) $q\bar{q}$ -nucleon cross section σ_{VN} (Eq.(8)) which enter the calculations [10]. Since the latter is slightly smaller, the real photon interacts with less nucleons than the pion.

Furthermore, $\langle \nu_t \rangle$ decreases with the photon virtuality at fixed energy. There are two main effects being responsible for this behavior:

- (i) Due to the $1/(M^2 + Q^2)$ -behavior of σ_{VN} this cross section decreases with Q^2 at fixed M^2 and fixed energy. Moreover, at large photon virtualities interactions of resolved photons with large masses M^2 become more important leading to a further decrease of the cross section σ_{VN} and therefore $\langle \nu_t \rangle$.
- (ii) The fraction of events with point-like photon interactions ($\nu_t = 1$) increases with rising photon virtuality.

As an example, this is shown in Fig. 5a for photon-copper interactions at a photon-nucleon c.m. energy of 150 GeV, an energy which could be available in the future for photon-nucleus collisions at HERA [46]. In our model, the average heavy particle multiplicity is approximately proportional to ν_t irrespectively of the nature of the projectile. This dependence is shown in Fig. 5b for protons, pions, real and weakly virtual photons ($Q^2 = 2 \text{ GeV}^2$). It reflects the fact that the number of heavy particles depends only on the number of nucleons “knocked out” of the target by the projectile and by subsequent intranuclear cascade processes and not on particular properties of the projectile-nucleon interactions [22, 23].

3.2.2 Average multiplicities

Average shower particle multiplicities in interactions of 150 GeV muons in emulsions are compared to data [47] in Fig. 6. Corresponding to the measurements, from the calculated events only those with more than two heavy particles in the final state have been taken into consideration. The flux of virtual photons is sampled according to the EPA and to the Q^2 -dependence of the photon-nucleus cross sections [10]. The multiplicities are shown as function of the inverse of the Bjorken- x . In this representation the average photon virtuality is decreasing from about 8 GeV² in the lowest bin ($1/x_{Bj} < 10$) to about 0.9 GeV² in the highest bin [47]. Our results agree with the data in the kinematic region of photoproduction ($Q^2 \lesssim 4 \text{ GeV}^2$, $1/x_{Bj} > 25$) but underestimate the data for higher virtualities. This fact may indicate that the PHOJET realization of the two-component DPM for photon-nucleon interactions fails in describing particle production in interactions of photons with relatively high virtualities at low energies. However, whereas the calculations are based in total on 50000 events one has to note that the data include about 17 events in each $1/x_{Bj}$ -bin [47]. Taking into account that these 17 events involve interactions with six different targets (emulsion

components) at different collision energies and photon virtualities one might conclude that the statistical significance of the data is limited.

Finally, we compare our results on multiplicities in muon–deuterium and muon–xenon interactions to data of the E665-Collab. [48]. The experiments were performed with a 490 GeV positive muon beam. The kinematic region under investigation is $Q^2 > 1 \text{ GeV}^2$, $8 < W < 30 \text{ GeV}$, $x_{\text{Bj}} > 0.002$, and $0.1 < \nu/E_\mu < 0.85$ (with ν being the photon energy in the laboratory). Furthermore, only charged particles with momenta $p > 200 \text{ MeV}/c$ in the laboratory frame are considered. We note that although the distribution of photons in leptons decreases with increasing Q^2 still a considerable fraction of all events is characterized by photons with rather large virtualities. These events cannot be expected to be described reliably within the present approach. In Figs. 7a and 7c the energy dependence of the average total, positively and negatively charged hadron multiplicities are shown. For both target nuclei the data are well reproduced by the model. The multiplicities of charged hadrons are shown separately for the forward and backward region of the photon–nucleon c.m. frame in Figs. 7b and 7d. The calculated multiplicities in the backward region which are strongly affected by target associated particle production and, therefore, by the laboratory momentum cut applied to the final state hadrons, are slightly higher than the data whereas those in forward direction are lower. Multiplicities averaged over all energies of the photon–nucleus interaction are compared to the corresponding experimental values in Table 2.

3.2.3 Inclusive particle distributions

In Fig. 8 the model results for the pseudorapidity distributions of shower particles from muon–emulsion interactions at 150 GeV are compared to data again from measurements by Hand *et al.* [47]. The kinematic range of the experiment is $0.6 < Q^2 < 21 \text{ GeV}^2$ and $2.5 < W \leq 16.5 \text{ GeV}$. The distributions shown for muon–emulsion interaction cover different but overlapping W -ranges: in a) data and MC results are plotted for $9 < W < 14 \text{ GeV}$ and in b) for $W > 10 \text{ GeV}$ ($\langle Q^2 \rangle = 2.7 \text{ GeV}^2$). Let us first compare the two data sets which include 43 events in a) and 47 events in b) [47]. One obvious difference is the peak in the distribution in a) at $\eta = 1.25$ which is not present in b). The only energy range which is not covered by the data in Fig. 8a as compared to 8b is $9 < W < 10 \text{ GeV}$. Therefore, we assume that this peak is due to statistical uncertainties within the experiment (c.f. also our discussion in Sect.3.2.2). Comparing the model results to the data we note that agreement within the statistical errors is obtained for $\eta > 2$. Disregarding the above mentioned peak, at lower pseudorapidities we underestimate the measured distributions slightly. Furthermore the comparison suggests that both, the measured and calculated distributions, agree in normalization (i.e. in the average multiplicity of shower particles) but the maximum of the calculated distribution appears at somewhat higher pseudorapidities than the measured one. In order to understand this discrepancy we compare in Fig. 8a in addition results for pion–emulsion interactions at 60 GeV to data [49]. This energy corresponds to the average photon laboratory energy of the distribution for the muon projectile in this Figure. The cuts on both data sample are similar: only events with at least three heavy particles are considered and shower particles are defined by their Lorentz- β value as $\beta > 0.7$. Our results for π^- –emulsion interactions agree in shape and in position of the maximum to the data. Therefore and with respect to conclusions from

comparisons with data drawn further below we attribute the discrepancy in the position of the maximum to the statistical uncertainties of the experiment.

Turning again to muon–deuterium and muon–xenon interactions at 490 GeV we compare in Figs. 9 and 10 rapidity distributions of positively (a) and negatively charged hadrons (b) in the photon–nucleon c.m. frame to data [48]. The comparisons are shown for three ranges of the photon–nucleon c.m. energy W . Taking into account that the treatment of high Q^2 -values in our model [15] might be too simplified, the description of the data by the model is satisfactory with the exception of the production of positively charged particles in the target fragmentation region of the muon–xenon interaction (Fig. 10a, $y \approx -3$). The peak in the calculated distributions clearly reflects the production of target associated particles by intranuclear cascade processes which are present in the distributions if a momentum cut as low as 200 MeV/ c in the laboratory frame is applied to the results. The multiplicity seen in the target fragmentation region depends strongly on this cutoff. We assume that the differences might be due to additional kinematic cuts applied to the data or due to experimental uncertainties (with respect to the momentum cutoff) for the following reasons: (i) the models for slow particle production implemented in DTUNUC 2.0 are in good agreement with data from hadron–nucleus as well as nucleus–nucleus collisions [22, 23], (ii) the dependence of shadowing on the photon virtuality and energy is qualitatively understood within our model and describes corresponding data of the E665-Collab. reasonably well [10], and (iii) the rapidity distributions of negatively charged particles and of positively charged particles outside the target fragmentation region in muon–xenon interactions and of charged particles in muon–deuterium interactions agree with E665-data.

Distributions of charged hadrons from muon–deuterium and muon–xenon interactions at 490 GeV were measured as function of $z = E/\nu$ (E and ν being the secondary hadron energy and the photon energy in the target rest frame, resp.) by Adams *et al.* [50]. In Figs. 11a and 11b our results on the z -distributions are shown together with these data. Both, model results and data, are restricted to the shadowing region, i.e. to $x_{Bj} < 0.005$ and $Q^2 < 1$ GeV². We find a good agreement in the whole z -range.

Feynman- x distributions are usually studied in terms of the one-particle inclusive variable $F(x_F)$ defined as

$$F(x_F) = \frac{1}{\sigma_{\gamma A}^{\text{tot}}} \frac{2E}{\pi W} \frac{d\sigma}{dx_F}, \quad x_F = \frac{2p_{\parallel}}{W}. \quad (10)$$

The quantities E , p_{\parallel} , and $W = \sqrt{s}$ denote the energy and longitudinal momentum in the photon–nucleon c.m. system, and the photon–nucleon c.m. energy, resp. The Feynman- x distribution of positively and negatively charged hadrons is given together with data [51] in Fig. 11c for muon–deuterium interactions at 147 GeV. Here, the photon virtualities are restricted to the range $0.5 < Q^2 < 3$ GeV² and the photon–nucleon c.m. energies to $W > 10$ GeV.

Finally, we compare in Fig. 12a the transverse momentum distributions of charged particles in different ranges of x_F again to data on muon–deuterium interactions from Ref. [51]. Our results are presented as histograms whereas fits to measured p_{\perp} -distributions are shown as continuous lines. The experimental uncertainties are increasing with p_{\perp} and are at least of the order of the differences between the fits for positive and negative particles [51]. They do not allow to draw conclusions concerning the disagreement between model predictions and data

at large transverse momenta. The dependence of the average transverse momenta of charged particles on x_F is shown in Fig. 12b.

3.2.4 The nuclear dependence of particle production

In order to study the dependence of particle production on the mass number A of the nuclear target, inclusive single particle cross sections, like pseudorapidity ($d\sigma/d\eta$), transverse momentum ($d\sigma/dp_\perp^2$), or Feynman- x distributions ($d\sigma/dx_F$), are usually fitted to a A^α -behavior. In the projectile fragmentation region of photon-nucleus collisions we expect α to approach unity (i) for small $q\bar{q}$ -nucleon cross sections, such as at low energies or for $Q^2 > 0$, (ii) at high energies for interactions becoming more point-like, and (iii) at large transverse momenta due to hard interactions. In the fragmentation region of the target nucleus α can exceed the value of one due to the formation zone intranuclear cascade, an effect being outside the scope of the present paper. Here, we restrict our discussion to the photon fragmentation region.

In Fig. 13 we show fits to results of the model on interactions of real and weakly virtual photons ($Q^2 = 1 \text{ GeV}^2$) with carbon, aluminum, copper, silver, xenon, and gold. Only charged particles with Lorentz- $\beta > 0.7$ (shower particles) are taken into consideration. The dependences of α on the pseudorapidity (a), on the transverse momentum (b), and on the Feynman- x variable (c) are plotted for a laboratory energy of 250 GeV. At all values of the studied variables α is larger for virtual than for real photon projectiles. This stronger A -dependence of the cross sections for virtual photons is due to the Q^2 -dependence of the effective $q\bar{q}$ -nucleon cross sections σ_{VN} (Eq.(8)). It demonstrates that the previously discussed property of the model, the Q^2 -dependence of shadowing (see Fig. 5), is clearly visible also in inclusive particle distributions. It might be interesting to study this effect also experimentally.

3.3 Jet photoproduction off nuclei at HERA-energies

Studying jet production in direct and resolved photon events in γp interactions striking differences have been observed by the experiments [5, 8, 9]. Therefore one can expect to observe similar effects when comparing point-like and resolved photon processes in photon-nucleus interactions. In the following, properties of hadronic jets produced in interactions of real photons with nuclei are studied at energies which might be reached with nuclear beams at HERA. Assuming nuclei with equal numbers of protons and neutrons the nuclear beam will have an energy per nucleon of 410 GeV [46]. With an average photon energy of about half of the electron energy (27.6 GeV) the photon-nucleon c.m. energy will be about 150 GeV.

Before discussing jet production let us first compare transverse momentum distributions of charged particles in proton- and photon-nucleus collisions. They very clearly reflect differences between interactions with proton and the photon projectiles which are responsible for characteristic features of jet production in photon-nucleus collisions. As shown in Fig. 14 the p_\perp -distribution of charged particles for photon-projectiles exhibits a less rapid decrease and extends to higher transverse momenta than the one for hadron projectiles. This property was already discussed in [15] comparing hadron-hadron, photon-hadron, and photon-photon interactions. The reasons are (i) the photon may interact in direct processes, and (ii) the photon PDFs are “harder” as compared to the proton PDFs.

As it has been shown in the analysis of data from HERA on photon–proton collisions [52] the study of jet production may give evidence for the subdivision into direct and resolved photon interactions. Therefore it can be expected that differences between hadron–nucleus and photon–nucleus collisions and characteristic features of point-like photon interactions emerge most clearly in a study of jet production. In the following, all observables used refer to the photon–nucleon c.m. system. Particle jets are defined according to the Snowmass-convention [53]. In the plane of pseudorapidity η and azimuthal angle ϕ a jet is defined as a collection of particles contained in a cone of radius $R = \sqrt{(\Delta\eta)^2 + (\Delta\phi)^2} = 1$. The jet transverse energy E_{\perp}^{jet} is taken as the sum of the particle transverse energies inside the cone. The jet pseudorapidity η^{jet} is calculated as E_{\perp} -weighted average over the pseudorapidities of the particles belonging to the jet.

In Fig. 15a we compare the transverse energy distributions of jets from proton–carbon and photon–carbon interactions. Similar to proton/photon–proton interactions [15], the E_{\perp}^{jet} distribution extends to higher transverse energies for photon–nucleus collisions as compared to proton–nucleus collisions. Differences between the two channels are even more pronounced within the pseudorapidity distributions of the jet axes. This is shown in Fig. 15b for jets with transverse energies higher than 6 GeV and 10 GeV. As initially mentioned, since the PDFs of the photon are harder than the PDFs of the proton and due to the point-like photon interactions we obtain in photon–nucleus collisions considerably more jets in forward direction ($\eta^{\text{jet}} > 0$). In backward direction the soft underlying event, being more pronounced for proton projectiles, is responsible for a higher jet rate.

The kinematic regions of jets from direct and resolved photon interactions might be separated if jet production is analysed as function of

$$x^{\text{obs}} = \frac{E_{\perp}^{\text{jet1}} e^{\eta^{\text{jet1}}} + E_{\perp}^{\text{jet2}} e^{\eta^{\text{jet2}}}}{2E_{\gamma}}. \quad (11)$$

E_{γ} denotes the photon energy. x^{obs} can be considered as an estimate for the fraction of the projectile momentum entering the hard scattering [8, 54]. In Fig. 16a we show x^{obs} -distributions for proton–carbon, photon–carbon, and photon–sulfur interactions. Point-like photon interactions contribute exclusively to the region $x^{\text{obs}} > 0.6$. The specific properties of jets and of the underlying event are usually studied in terms of jet profiles. This is shown for photon–carbon interactions and different x^{obs} -bins in Fig. 16b where we plot the average transverse energy as a function of the distance in pseudorapidity from the jet axis. Since in direct photon interactions there is no photon remnant which could contribute to the jet pedestal, the transverse energy outside the jets is decreasing with increasing x^{obs} . Of course, as the mass number of the target nucleus increases the soft underlying event becomes more pronounced, i.e. the average transverse energy of the jet pedestal increases. This is demonstrated in Fig. 16c for four different target nuclei. Here, all jets with $E_{\perp} > 6$ GeV are included.

4 Summary and conclusions

The two-component Dual Parton Model is applied to multiparticle photoproduction off nuclei. By incorporating the PHOJET event generator for hadron–nucleon and photon–nucleon

interactions, it is now possible to describe with the event generator DTUNUC 2.0 consistently cross sections and particle production in high energy hadron–nucleus, real and weakly virtual photon–nucleus, and nucleus–nucleus collisions (the latter are not discussed in this paper).

In [10] it has been shown that the model correctly describes the shadowing behavior of high energy photon–nucleus cross sections. Based on this fact and on the overall good agreement of model results and data in all main aspects of particle production in photon–hadron and hadron–nucleus collisions no further freedom exists in the model for its application to multi-particle photoproduction off nuclei. It is therefore a severe test of the model. Unfortunately, only a few data are available in the kinematic region $Q^2 \ll s$, $Q^2 < 9 \text{ GeV}^2$ to which the predictions of DTUNUC 2.0 can be compared. As discussed in this paper, model results are qualitatively consistent with many features of these data.

Within the model the photon is treated (i) as a resolved $q\bar{q}$ -state interacting with target nucleons according to the GVDM and the Gribov–Glauber approximation in multiple soft and hard scattering processes and (ii) as a point-like object interacting in a single hard scattering with one target nucleon (anomalous component of the photon PDF and direct photon interactions). On the basis of this treatment we obtain the following results:

- As expected from studies of photon–nucleus cross sections, also particle production off nuclei clearly shows decreasing shadowing with increasing photon virtualities.
- At energies of present fixed target experiments, inclusive single particle cross sections become proportional to A^α , $\alpha \approx 1$, already at $Q^2 > 1 \text{ GeV}^2$ due to decreasing $q\bar{q}$ -nucleon cross sections with increasing Q^2 . However, more data on particle production in photon–nucleus collisions would be needed for a detailed investigation of the transition region.
- In analogy to observations in photon–proton collisions at HERA we argue that also in photoproduction off nuclei the dual nature of the photon and, therefore, point-like photon interactions show up most clearly in hadronic jet production. As examples we present transverse energy and pseudorapidity distributions of jets and we study jet profiles in real photon–nucleus collisions at energies which might be reached with nuclear beams at HERA. The strong dependence of the jet profiles and of the underlying event on the fraction of the momentum of the photon going into jets which was first observed at HERA, can be expected to be present also in photon–nucleus collisions.

Acknowledgements

Discussions with F. W. Bopp are gratefully acknowledged. One of the authors (J.R.) thanks C. Pajares for the hospitality at the University Santiago de Compostela and he was supported by the Direccion General de Politicia Cientifica of Spain. One of the authors (R.E.) was supported by the Deutsche Forschungsgemeinschaft under contract No. Schi 422/1-2.

References

- [1] M. Drees and R. M. Godbole, *Pramana J. Phys.* **41**, 83 (1993).
- [2] M. Drees and R. M. Godbole, *J. Phys.* **G21**, 1559 (1995).
- [3] T. H. Bauer, R. D. Spital, and D. R. Yennie, *Rev. Mod. Phys.* **50**, 261 (1978).
- [4] H. Kolanoski and P. Zerwas, *Two-photon physics*, (World Scientific, Singapore, 1988), in: High energy electron-positron physics, ed. by A. Ali and P. Söding.
- [5] R. Tanaka *et al.*, *Phys. Lett.* **B277**, 215 (1992).
- [6] T. Ahmed *et al.*, *Phys. Lett.* **B297**, 205 (1992).
- [7] M. Derrick *et al.*, *Phys. Lett.* **B322**, 287 (1994).
- [8] S. Aid *et al.*, *Z. Phys.* **C70**, 17 (1995).
- [9] M. Derrick *et al.*, *Phys. Lett.* **B354**, 136 (1995).
- [10] R. Engel, J. Ranft, and S. Roesler, *Phys. Rev.* **D55**, 6957 (1997).
- [11] A. Capella, J. Trân Thanh Vân, and J. Kwieciński, *Phys. Rev. Lett.* **58**, 2015 (1987).
- [12] F. W. Bopp, R. Engel, D. Pertermann, and J. Ranft, *Phys. Rev.* **D49**, 3236 (1994).
- [13] P. Aurenche *et al.*, *Phys. Rev.* **D45**, 92 (1992).
- [14] R. Engel, *Z. Phys.* **C66**, 203 (1995).
- [15] R. Engel and J. Ranft, *Phys. Rev.* **D54**, 4244 (1996).
- [16] A. Capella, U. Sukhatme, C. I. Tan, and J. Trân Thanh Vân, *Phys. Rep.* **236**, 225 (1994).
- [17] J. Ranft, *Phys. Rev.* **D51**, 64 (1995).
- [18] R. J. Glauber, *Phys. Rev.* **100**, 242 (1955).
- [19] V. N. Gribov, *Sov. Phys. JETP* **30**, 709 (1970).
- [20] L. Bertochi, *Il Nuovo Cimento* **11A**, 45 (1972).
- [21] S. Y. Shmakov, V. V. Uzhinskii, and A. M. Zadoroshny, *Comp. Phys. Commun.* **54**, 125 (1989).
- [22] A. Ferrari, J. Ranft, S. Roesler, and P. R. Sala, *Z. Phys.* **C70**, 413 (1996).
- [23] A. Ferrari, J. Ranft, S. Roesler, and P. R. Sala, *Z. Phys.* **C71**, 75 (1996).
- [24] S. Aid *et al.*, *Z. Phys.* **C69**, 27 (1995).

- [25] S. Aid *et al.*, Nucl. Phys. **B463**, 3 (1996).
- [26] V. N. Gribov, Sov. Phys. JETP **26**, 414 (1968).
- [27] B. L. Combridge, J. Kripfganz, and J. Ranft, Phys. Lett. **B70**, 234 (1977).
- [28] V. A. Abramovski, V. N. Gribov, and O. V. Kancheli, Sov. J. Nucl. Phys. **18**, 308 (1974).
- [29] G. Veneziano, Nucl. Phys. **B117**, 519 (1976).
- [30] M. Glück, E. Reya, and A. Vogt, Phys. Rev. **D46**, 1973 (1992).
- [31] M. Glück, E. Reya, and A. Vogt, Z. Phys. **C53**, 127 (1992).
- [32] T. Sjöstrand, Comp. Phys. Commun. **39**, 347 (1986).
- [33] T. Sjöstrand and M. Bengtsson, Comp. Phys. Commun. **43**, 367 (1987).
- [34] A. Capella, U. Sukhatme, and J. Trân Thanh Vân, Z. Phys. **C3**, 329 (1980).
- [35] A. Capella, U. Sukhatme, C. I. Tan, and J. Trân Thanh Vân, Z. Phys. **C10**, 249 (1981).
- [36] A. B. Kaidalov, Phys. Lett. **B116**, 459 (1982).
- [37] A. B. Kaidalov and K. A. Ter-Martirosyan, Phys. Lett. **B117**, 247 (1982).
- [38] R. Engel, M. A. Braun, C. Pajares, and J. Ranft, Z. Phys. **C74**, 687 (1997).
- [39] H.-J. Möhring and J. Ranft, Z. Phys. **C52**, 643 (1991).
- [40] J. Ranft, A. Capella, and J. Trân Thanh Vân, Phys. Lett. **B320**, 346 (1994).
- [41] G. Grammer, Jr. and D. Sullivan, *Nuclear Shadowing of Electromagnetic Processes*, (Plenum Press,, New York,, 1978), in: Electromagnetic Interactions of Hadrons, Volume 2, ed. by A. Donnachie and G. Shaw.
- [42] E. Segré, *Nuclei and particles*, (Reading Mass,, Benjamin,, 1977).
- [43] K. Braune *et al.*, Z. Phys. **C17**, 105 (1983).
- [44] M. L. Cherry *et al.*, Phys. Rev. **D50**, 4272 (1994).
- [45] R. Albrecht *et al.*, Z. Phys. **C47**, 367 (1990).
- [46] M. Arneodo *et al.*, in Proceedings of the Workshop Future Physics at HERA 1995/96, ed. by G. Ingelman, A. De Roeck and R. Klanner, p. 887 (unpublished).
- [47] L. Hand *et al.*, Acta Phys. Pol. B **9**, 1087 (1978).
- [48] M. R. Adams *et al.*, Z. Phys. **C61**, 179 (1994).
- [49] J. Babecki *et al.*, Acta Physica Polonica **B9**, 495 (1978).

- [50] M. R. Adams *et al.*, Phys. Rev. **D50**, 1836 (1994).
- [51] W. A. Loomis *et al.*, Phys. Rev. **D19**, 2543 (1979).
- [52] M. Erdmann, *The Partonic Structure of the Photon*, Springer Tracts in Mod. Phys. 138, Heidelberg: Springer (1997).
- [53] J. E. Huth *et al.*, in Proceedings of the 1990 PDF Summer Study on High Energy Physics, Snowmass, Colorado, 1990, ed. by E. L. Berger, World Scientific, Singapore, p. 134 (unpublished).
- [54] T. Ahmed *et al.*, Nucl. Phys. **B445**, 195 (1995).

Tables

Table 1: Multiplicities of shower particles ($\beta > 0.7$) in interactions of pions and protons with carbon-, copper-, and lead-nuclei at 50, 100, and 150 GeV are compared to measurements [43].

	$E_{\text{Lab}}=50 \text{ GeV}$		$E_{\text{Lab}}=100 \text{ GeV}$		$E_{\text{Lab}}=150 \text{ GeV}$	
	DTUNUC 2.0	Exp.	DTUNUC 2.0	Exp.	DTUNUC 2.0	Exp.
$\pi^+ \text{-C}$	7.3	7.62 ± 0.14	9.0	9.19 ± 0.17	9.9	10.01 ± 0.18
$\pi^+ \text{-Cu}$	8.6	8.81 ± 0.23	10.5	10.41 ± 0.27	11.8	11.57 ± 0.30
$\pi^+ \text{-Pb}$	10.1	10.11 ± 0.38	12.2	11.54 ± 0.44	14.3	13.08 ± 0.50
p-C	7.7	7.88 ± 0.15	9.2	9.25 ± 0.18	10.3	10.58 ± 0.19
p-Cu	9.8	9.52 ± 0.24	11.9	11.40 ± 0.29	13.3	12.93 ± 0.33
p-Pb	11.1	11.31 ± 0.43	13.8		15.9	14.95 ± 0.57

Table 2: Results on average multiplicities of all charged $\langle N_{\text{ch}} \rangle$, positive $\langle N_+ \rangle$, negative $\langle N_- \rangle$, forward $\langle N_{\text{F}} \rangle$, and backward $\langle N_{\text{B}} \rangle$ hadrons ($p > 200 \text{ MeV}/c$) for muon–deuterium and muon–xenon interactions at 490 GeV are compared to data of the E665-Collab. [48].

	$\mu^+ \text{--D}_2$		$\mu^+ \text{--Xe}$	
	DTUNUC 2.0	Exp.	DTUNUC 2.0	Exp.
$\langle N_{\text{ch}} \rangle$	7.7	7.83 ± 0.07	10.8	9.99 ± 0.13
$\langle N_+ \rangle$	4.1	4.16 ± 0.05	6.8	6.00 ± 0.11
$\langle N_- \rangle$	3.6	3.67 ± 0.05	4.0	3.99 ± 0.06
$\langle N_{\text{F}} \rangle$	4.1	4.60 ± 0.05	4.2	4.70 ± 0.07
$\langle N_{\text{B}} \rangle$	3.6	3.23 ± 0.04	6.6	5.29 ± 0.11

Figure Captions

1. Color flow picture of a single reggeon exchange graph (a) and the corresponding unitarity cut (b). In c) and d) the same is shown for a single pomeron exchange.
2. Comparison of model results to data on pion–emulsion interactions [44]. In a) shower particle multiplicity distributions are shown for a laboratory energy of 525 GeV. In b) pseudorapidity distributions of shower particles are given for two different energies: 60 GeV and 525 GeV.
3. Model predictions on transverse momentum distributions of π^0 's in proton–gold interactions at 200 GeV are compared to data of the WA80-Collab. [45].
4. Average numbers of copper nucleons $\langle \nu_t \rangle$ struck by projectile pions, real and virtual ($Q^2 = 2 \text{ GeV}^2$) photons are given as function of the projectile laboratory energy (a). In b) and c) average multiplicities of shower $\langle N_s \rangle$ and heavy particles $\langle N_h \rangle$ are presented. Shower particles are defined as singly charged particles with $\beta > 0.7$. Heavy particles are charged particles with $\beta \leq 0.7$ except residual copper nuclei.
5. In a) the Q^2 -dependence of the average number of copper nucleons interacting with the photon $\langle \nu_t \rangle$ is given for a photon–nucleon c.m. energy of 150 GeV. In b) the dependence of the average heavy particle multiplicity on ν_t is shown for proton, pion, real photon, and weakly virtual photon ($Q^2 = 2 \text{ GeV}^2$) projectiles at the same energy.
6. Average numbers of charged hadrons ($\beta > 0.7$) in muon–emulsion interaction events at 150 GeV with more than two heavy particles in the final state are given as function of the inverse of the Bjorken- x variable and are compared to data [47].
7. The dependence of average multiplicities of charged hadrons on the squared energy of the virtual photon–nucleon c.m. system is shown for muon–deuterium (a,b) and muon–xenon interactions (c,d) at 490 GeV and is compared to measurements of the E665-Collab. [48]. In a) and c) we give the average multiplicities of all $\langle N_{\text{ch}} \rangle$, of positively $\langle N_+ \rangle$, and of negatively $\langle N_- \rangle$ charged hadrons. In b) and d) the average multiplicities of all charged hadrons are shown for positive $\langle N_F \rangle$ and negative $\langle N_B \rangle$ c.m. rapidities.
8. Pseudorapidity distributions of charged hadrons ($\beta > 0.7$) from muon–emulsion interactions at 150 GeV are shown together with data [47]. In a) the photon–nucleon c.m. energy range is restricted to $9 < W < 14 \text{ GeV}$. In addition, the pseudorapidity distribution of charged hadrons from pion–emulsion interactions at 60 GeV is plotted and compared to data [49]. In b) the results for $W > 10 \text{ GeV}$ are given. In both distributions only events with $N_h \geq 3$ are included.
9. Rapidity distributions of positive (a) and negative hadrons (b) from muon–deuterium interactions at 490 GeV are shown together with data [48] for different ranges of the virtual photon–nucleon c.m. energy W .
10. As in Fig. 9, here for muon–xenon interactions.

11. Energy- (z -) distributions of charged hadrons from muon–deuterium (a) and muon–xenon interactions (b) at 490 GeV are compared to measurements of the E665-Collab. [50]. Corresponding to the experimental cuts applied to the data the MC-results are restricted to $x_{\text{Bj}} < 0.005$, $Q^2 < 1 \text{ GeV}^2$, and $\nu > 100 \text{ GeV}$. In c) model results for Feynman- x distributions of charged hadrons from muon–deuterium interactions at $E_{\text{Lab}} = 147 \text{ GeV}$ are compared to data [51].
12. In a) transverse momentum distributions of charged hadrons from muon–deuterium interactions at 147 GeV are presented for different Feynman- x ranges. The model results (histograms) are plotted together with fits to data as given in [51]. In b) the x_{F} -dependence of the average transverse momenta of charged hadrons are compared to data [51].
13. The power α of the nuclear dependence of inclusive charged particle cross sections is shown as function of the pseudorapidity (a), the transverse momentum (b), and the Feynman- x variable (c) for real photon and weakly virtual photon projectiles of 250 GeV laboratory energy.
14. Transverse momentum distributions of charged hadrons from proton– and photon–carbon interactions at a proton/photon–nucleon c.m. energy of 150 GeV.
15. In a) transverse energy distributions are presented for hadronic jets from proton–carbon and real photon–carbon interactions at an energy of 150 GeV in the proton/photon–nucleon c.m. system. In b) the pseudorapidity distributions of the jet axes are shown for two lower cuts in transverse energy.
16. Dependence of jet production on the fraction of the projectile momentum carried by the jets (x^{obs}) at a proton/photon–nucleon c.m. energy of 150 GeV: In a) the x^{obs} -distributions of proton– and real photon–carbon and of real photon–sulfur interactions are plotted. Jet profiles as function of the distance in pseudorapidity from the jet axis are presented in b) for different x^{obs} -bins. In c) the jet profiles are shown for different target nuclei and all x^{obs} -values.

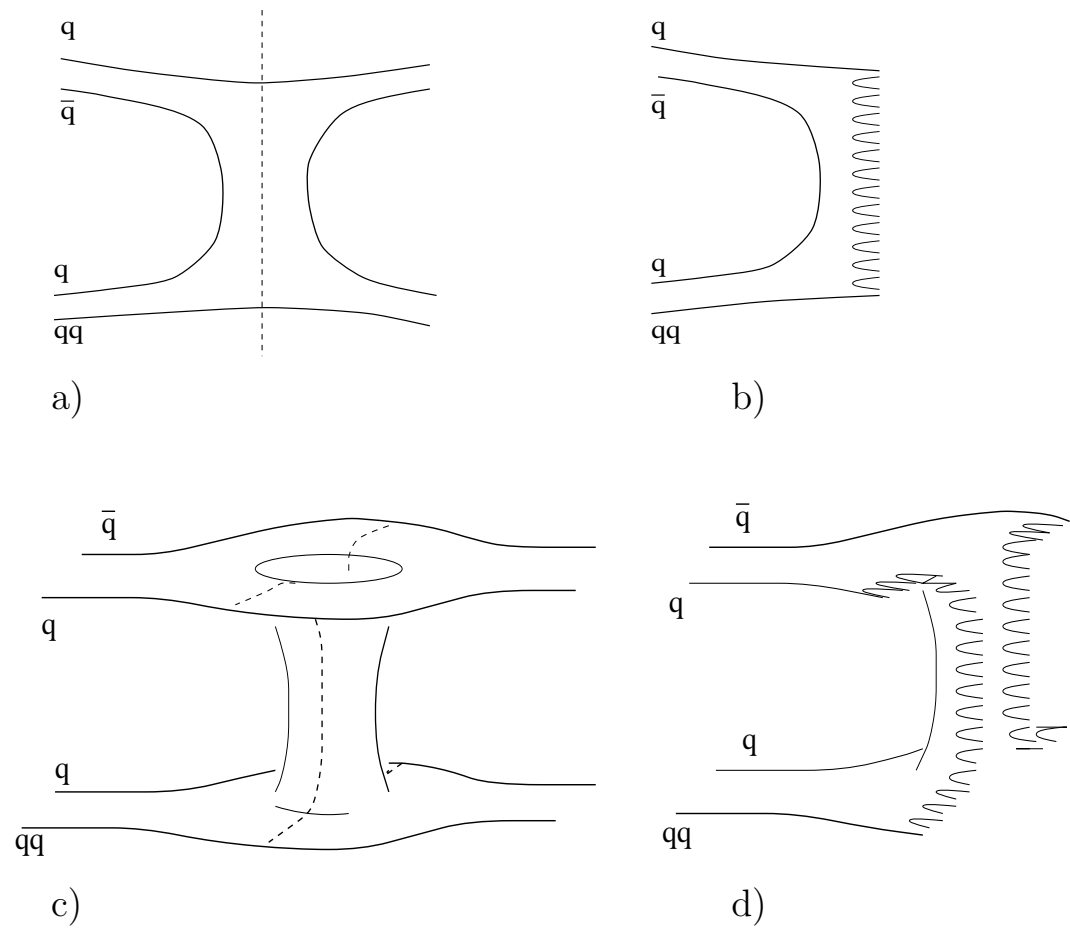
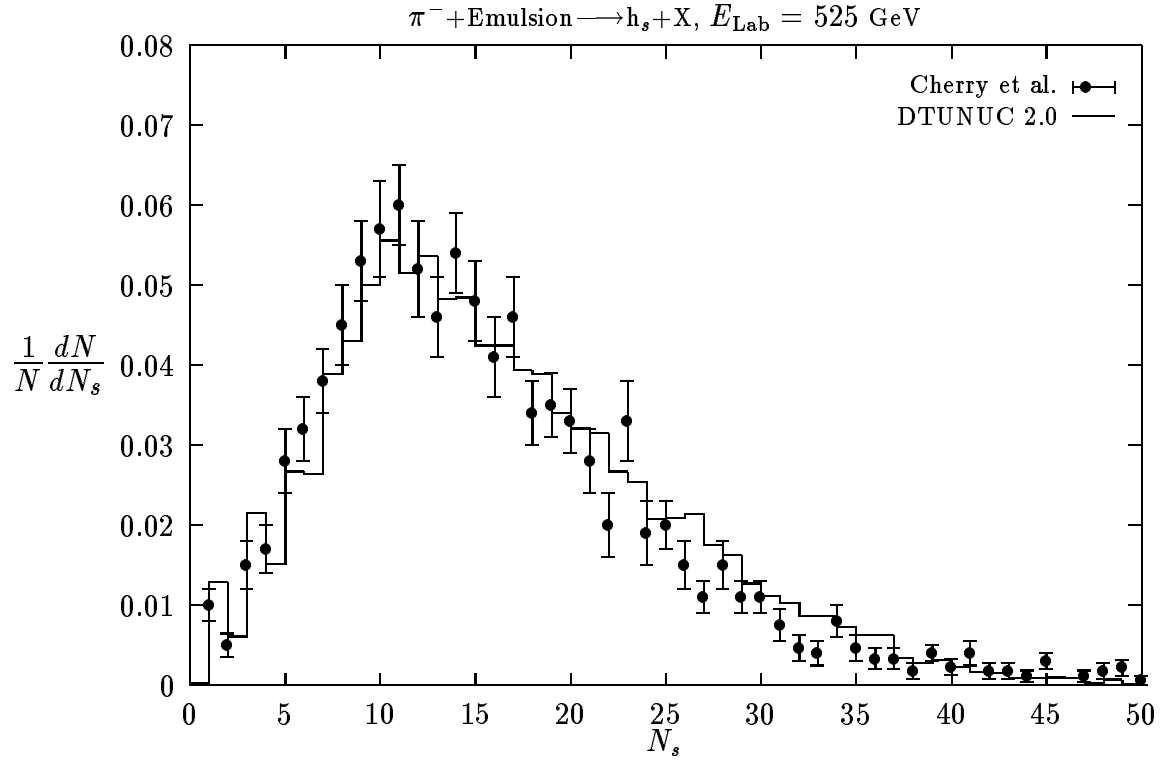
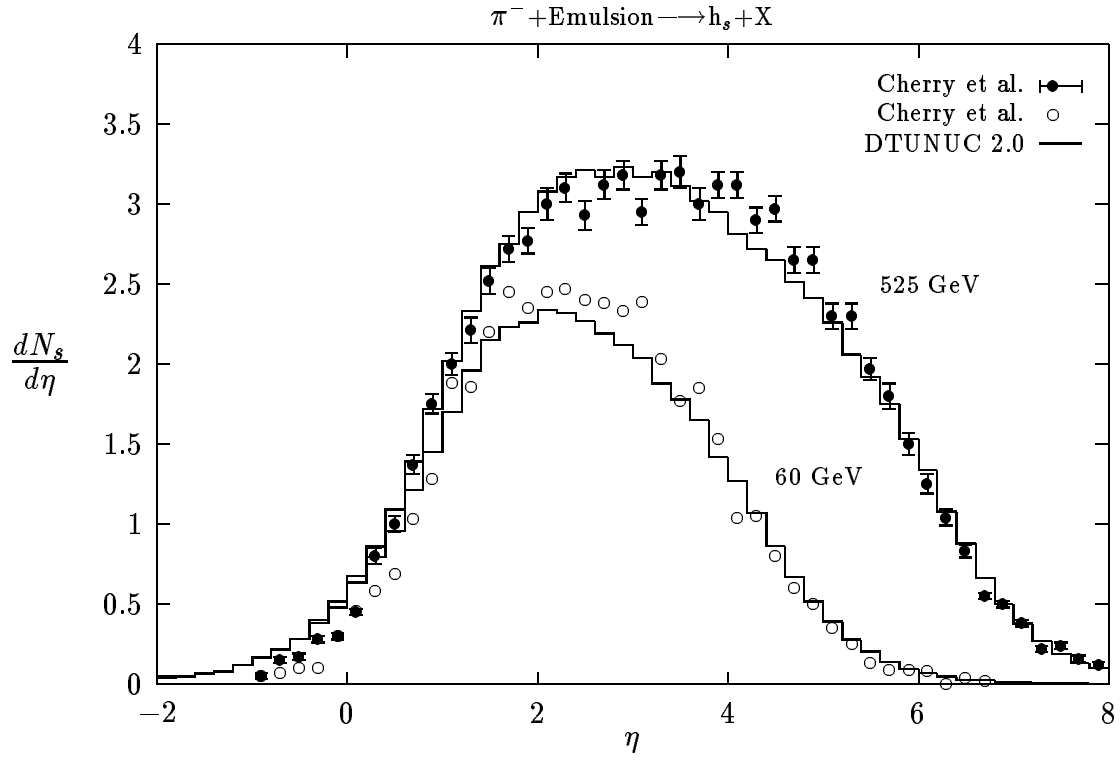


Fig. 1



a)



b)

Fig. 2

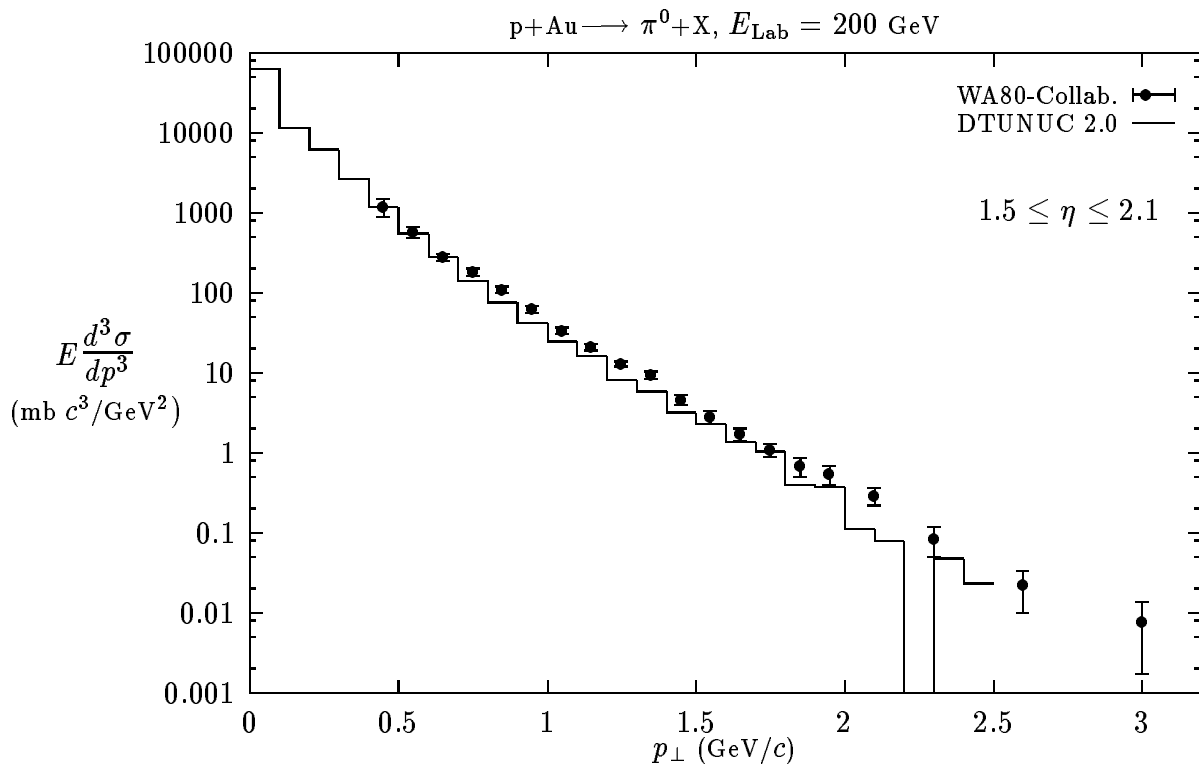


Fig. 3

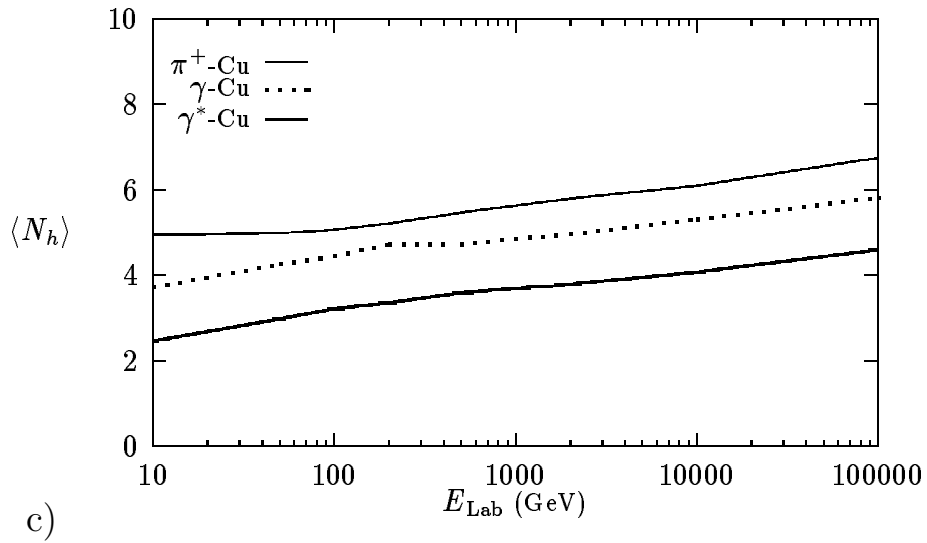
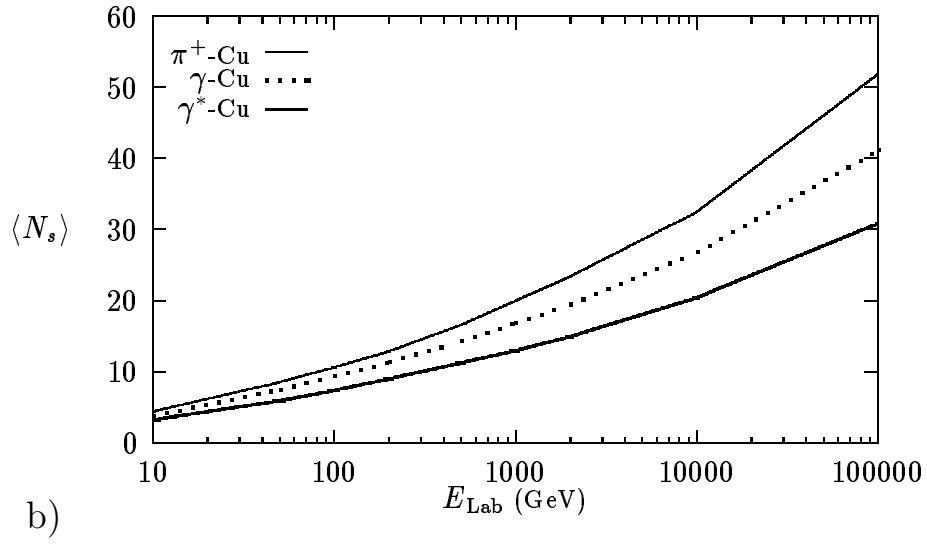
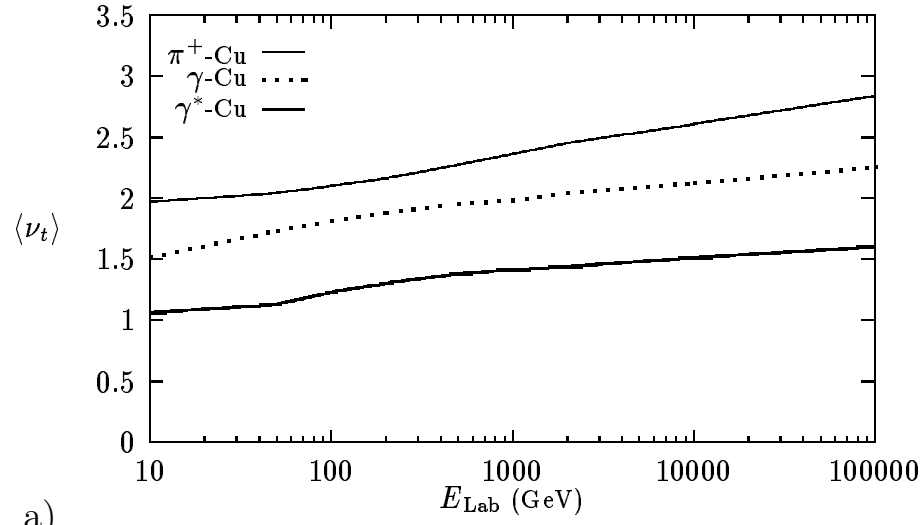
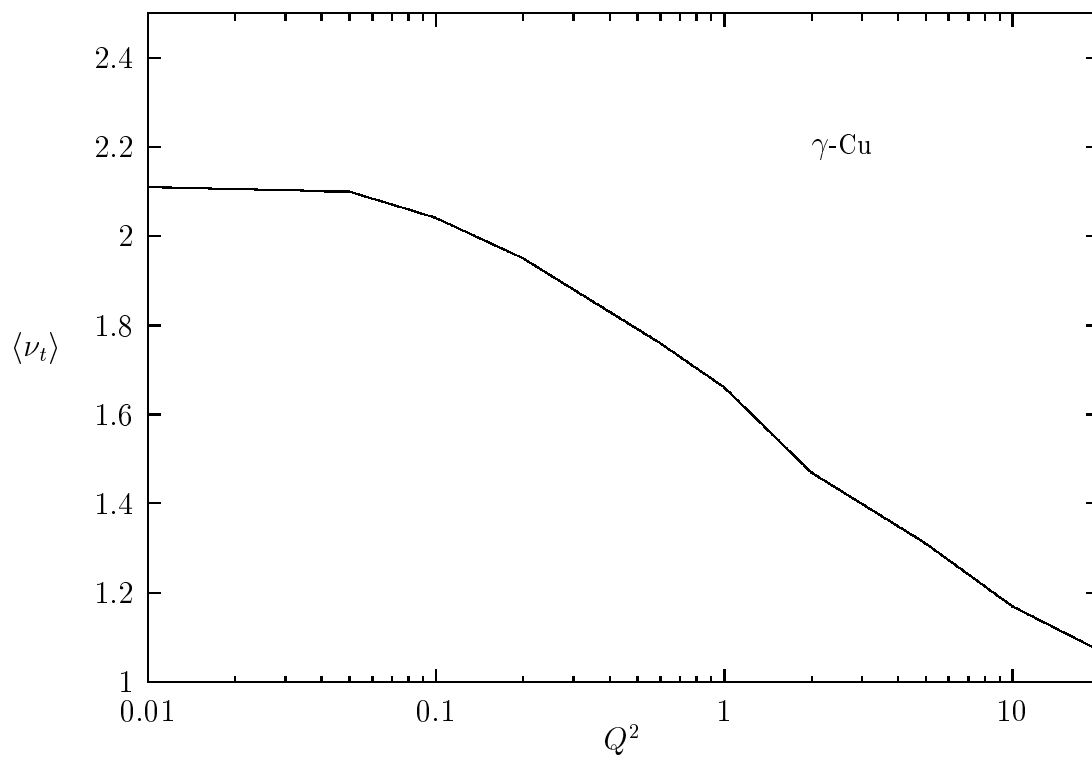
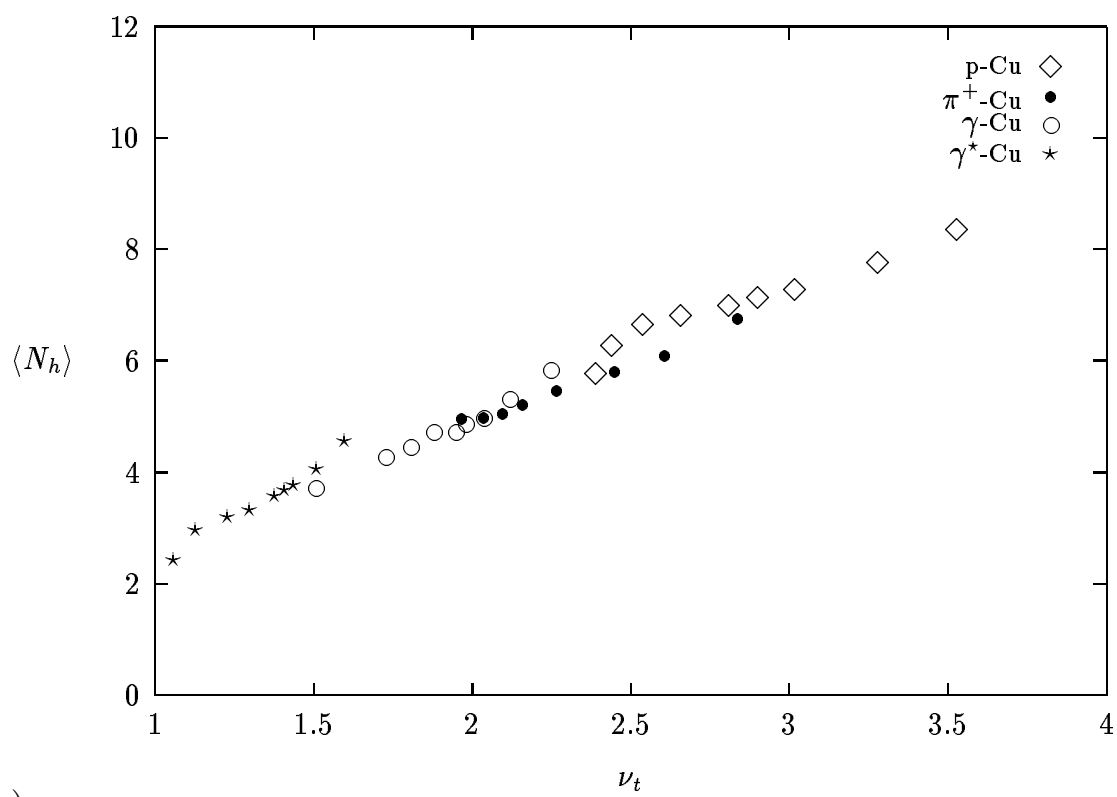


Fig. 4



a)



b)

Fig. 5

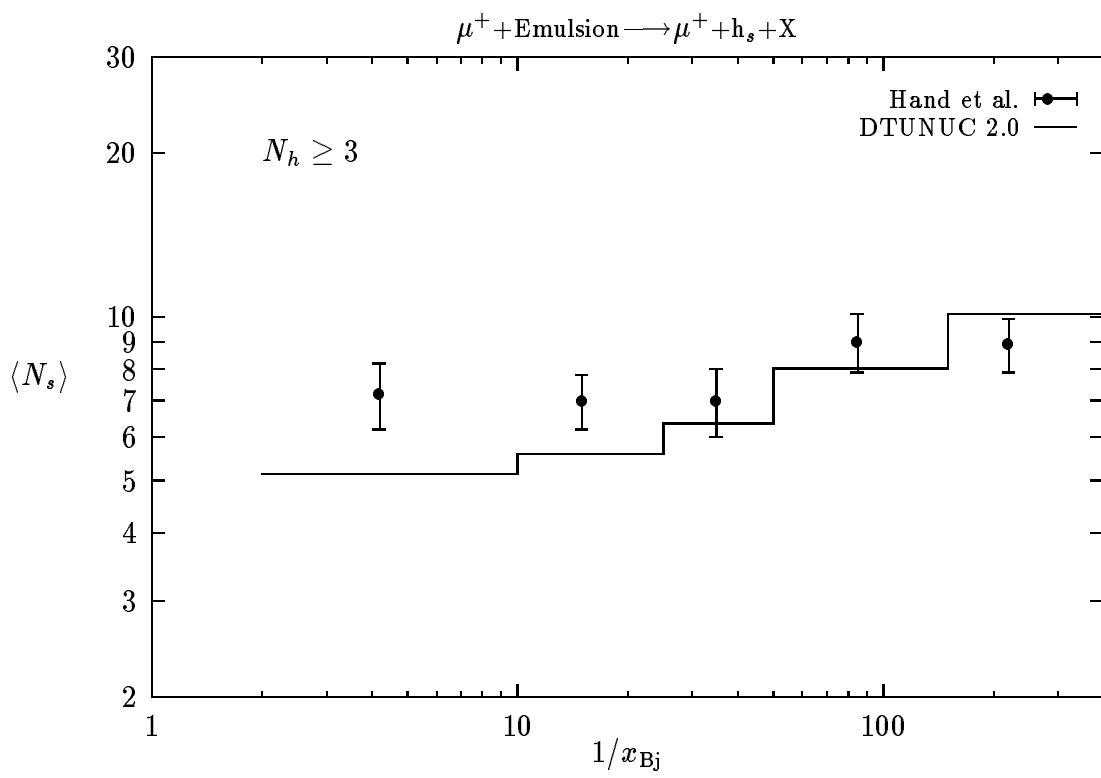


Fig. 6

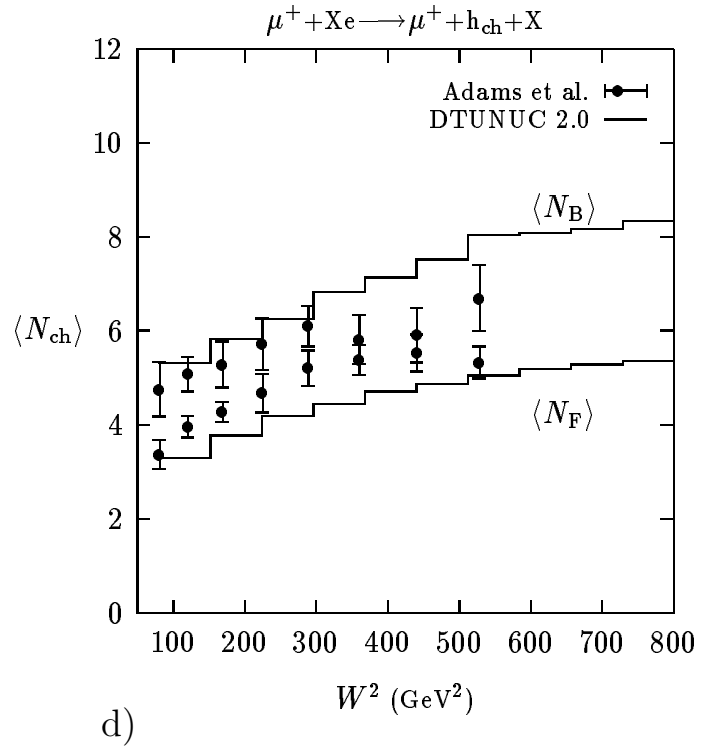
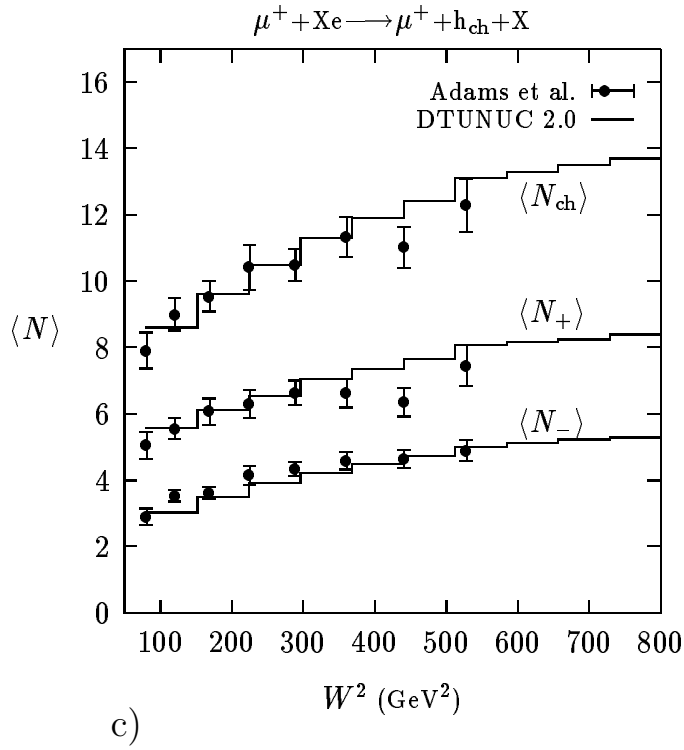
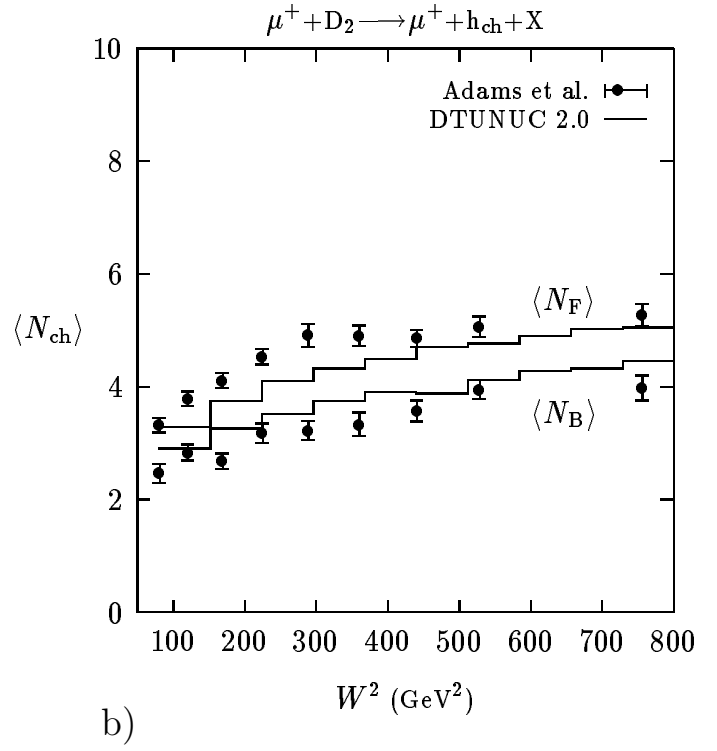
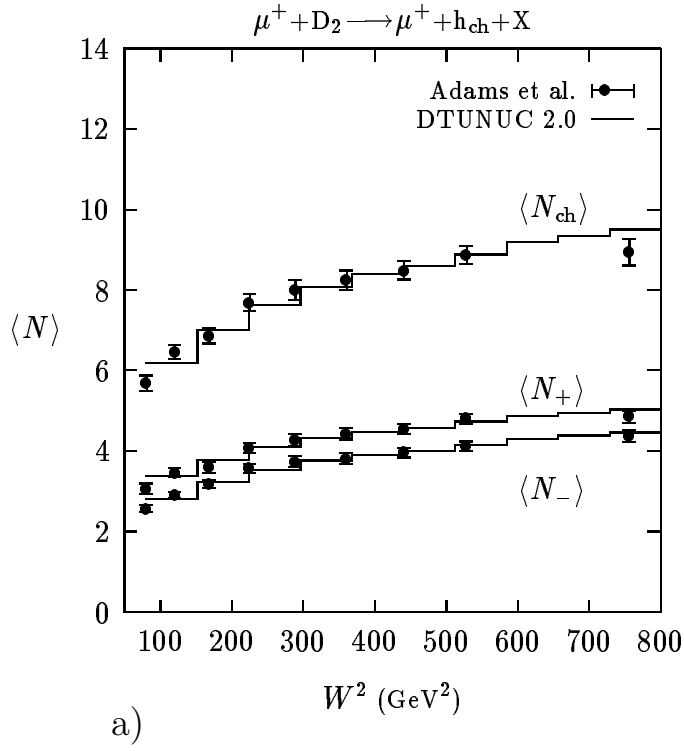
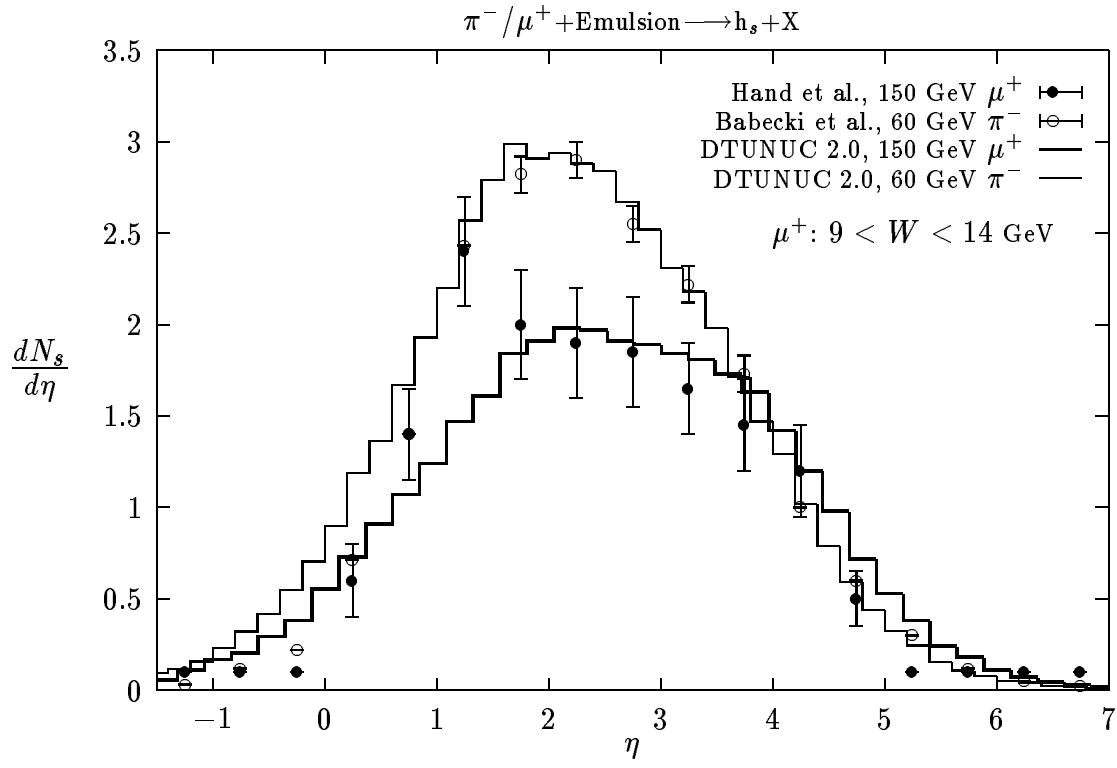
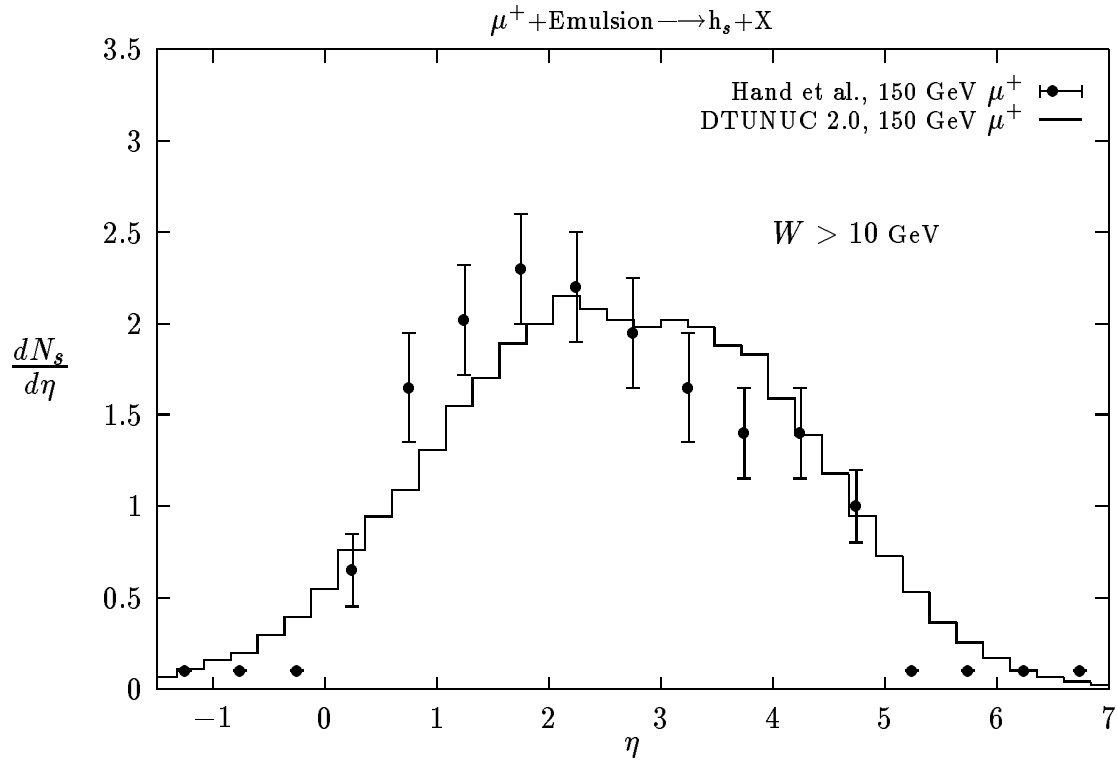


Fig. 7

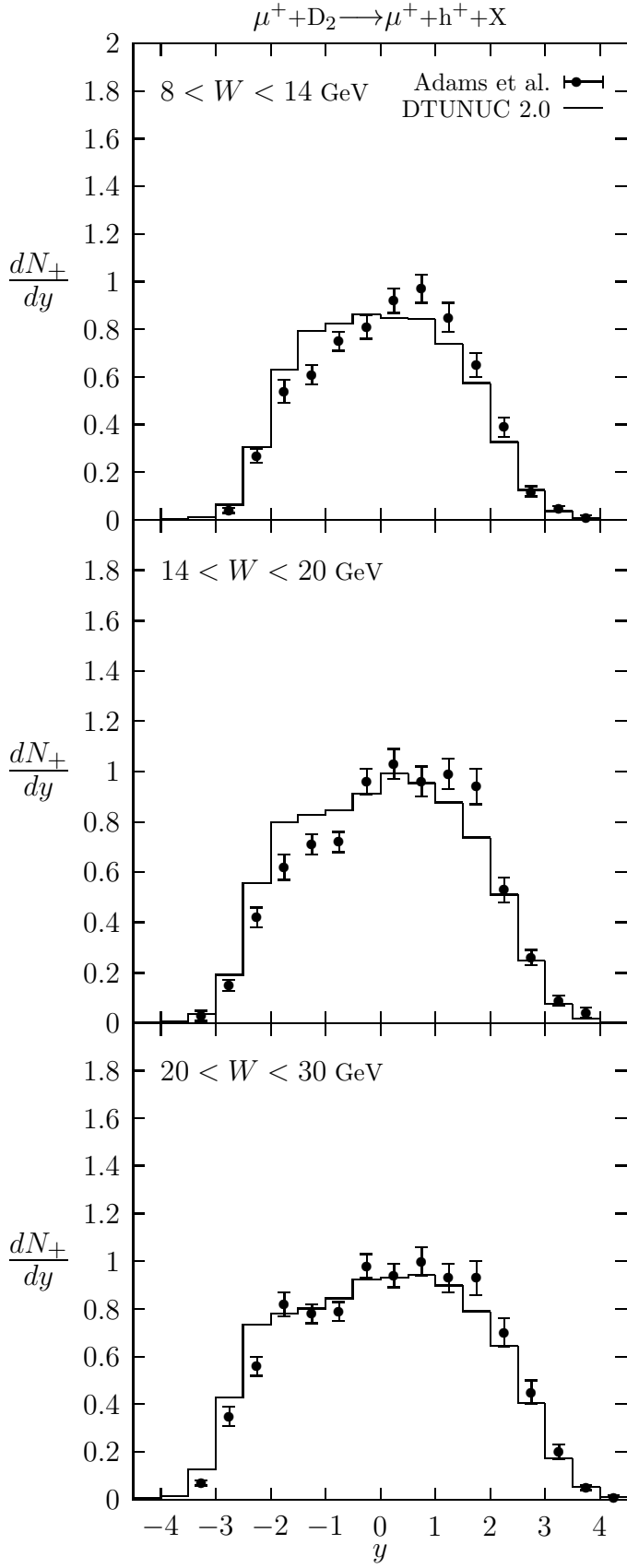


a)

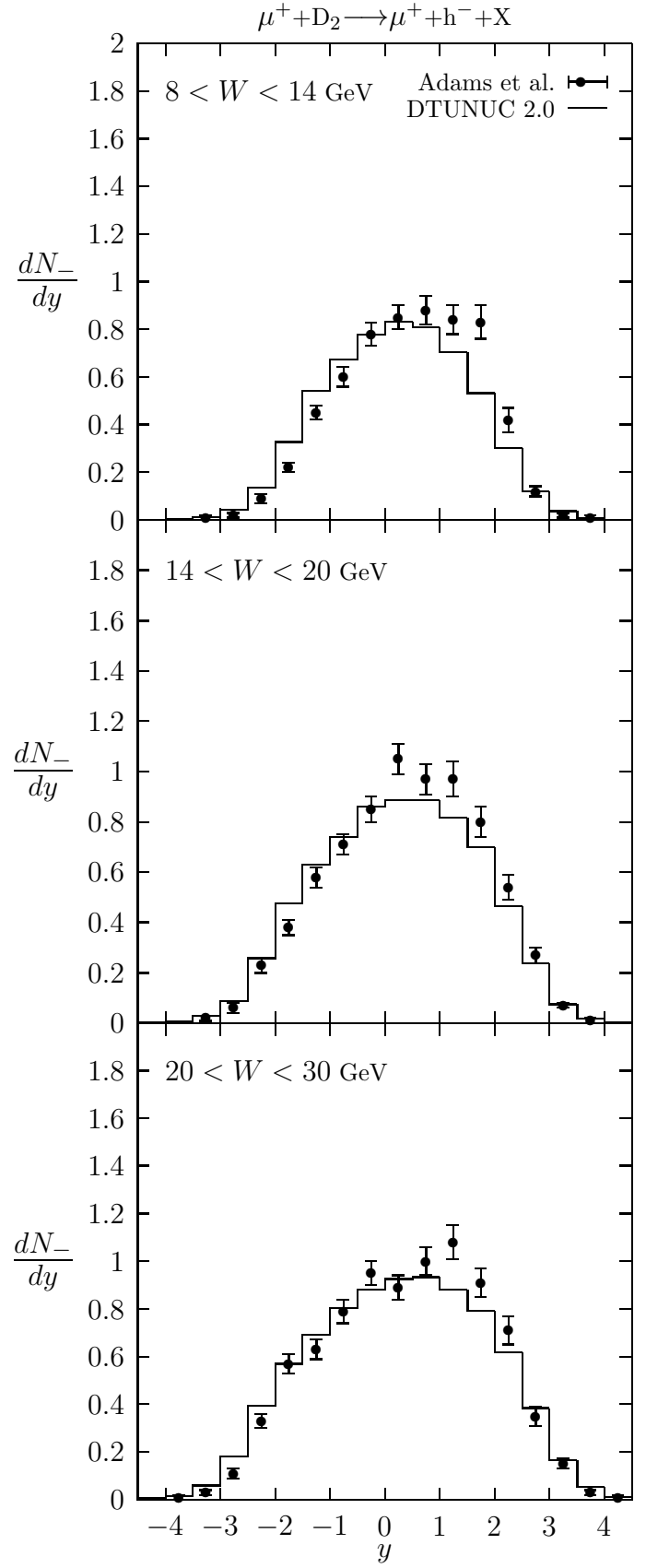


b)

Fig. 8

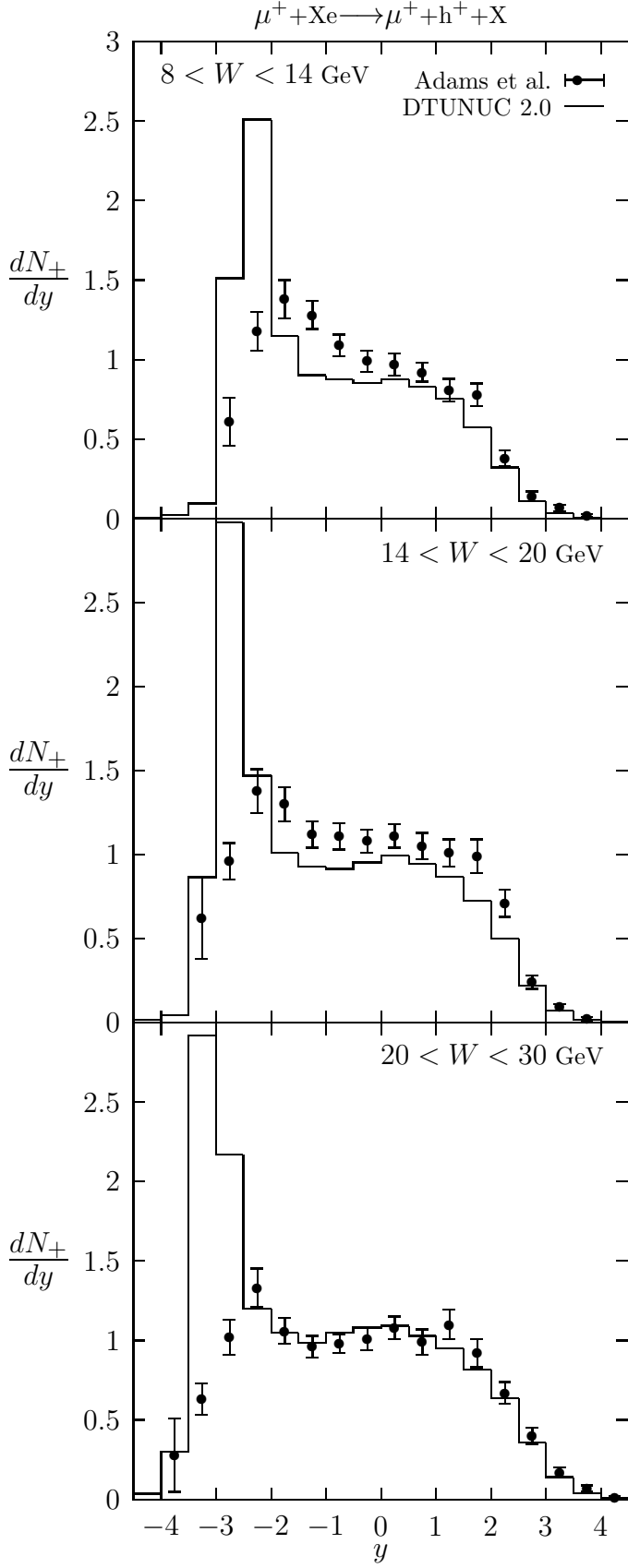


a)

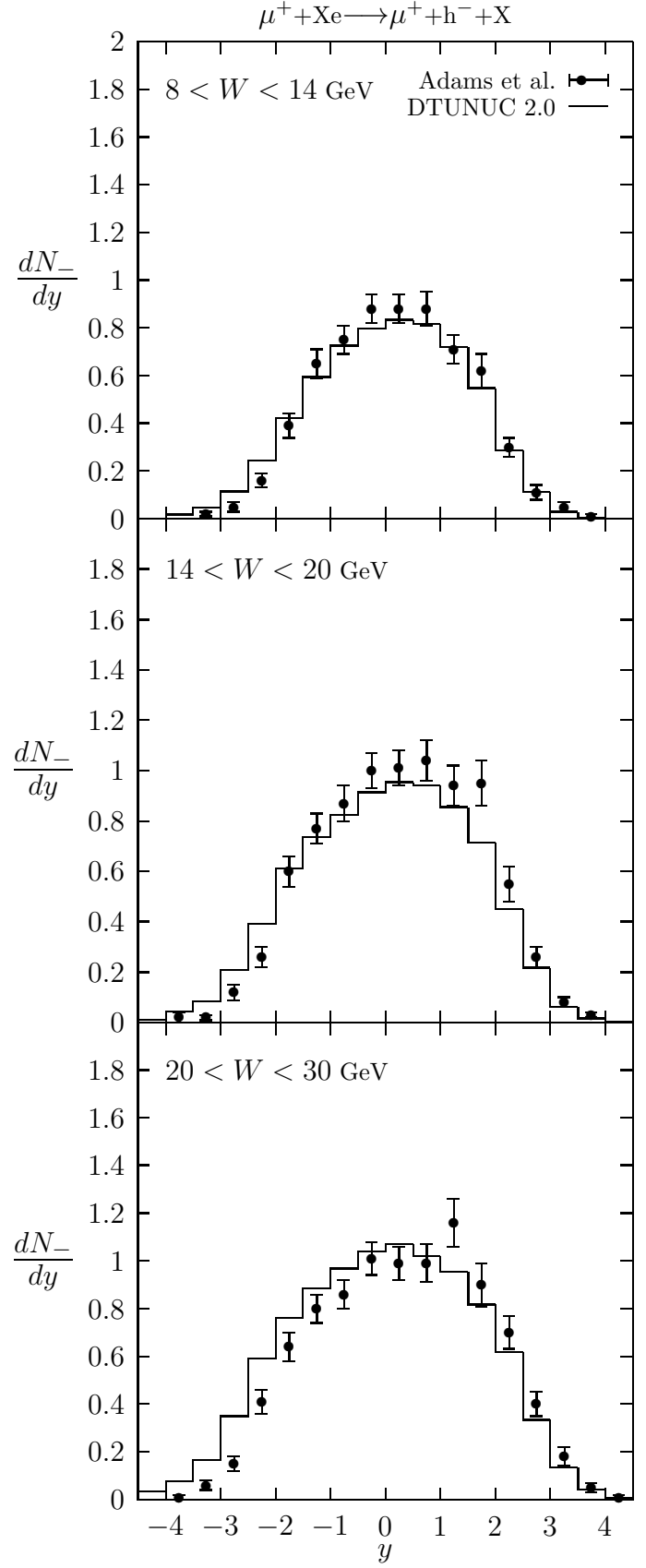


b)

Fig. 9

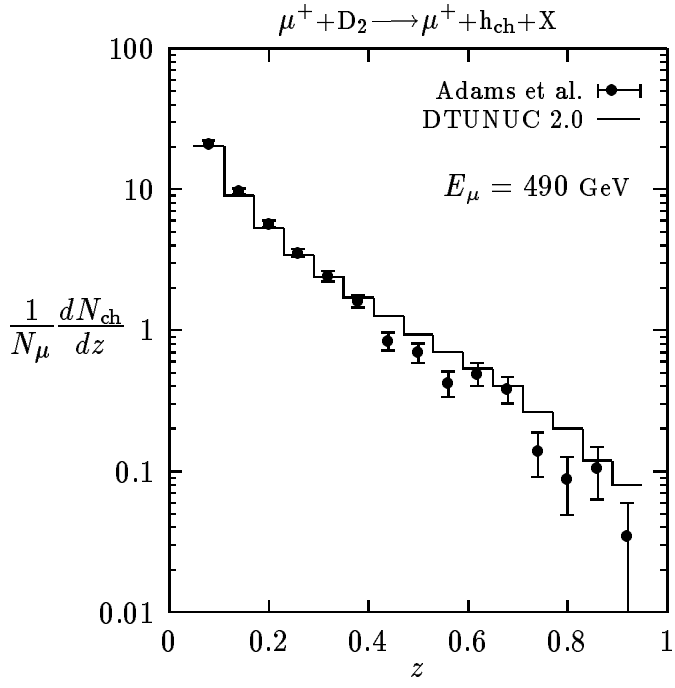


a)

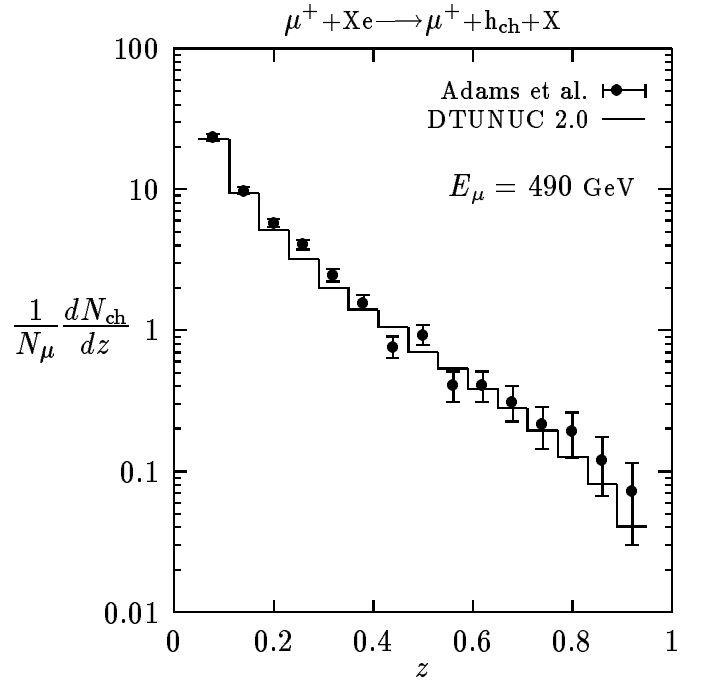


b)

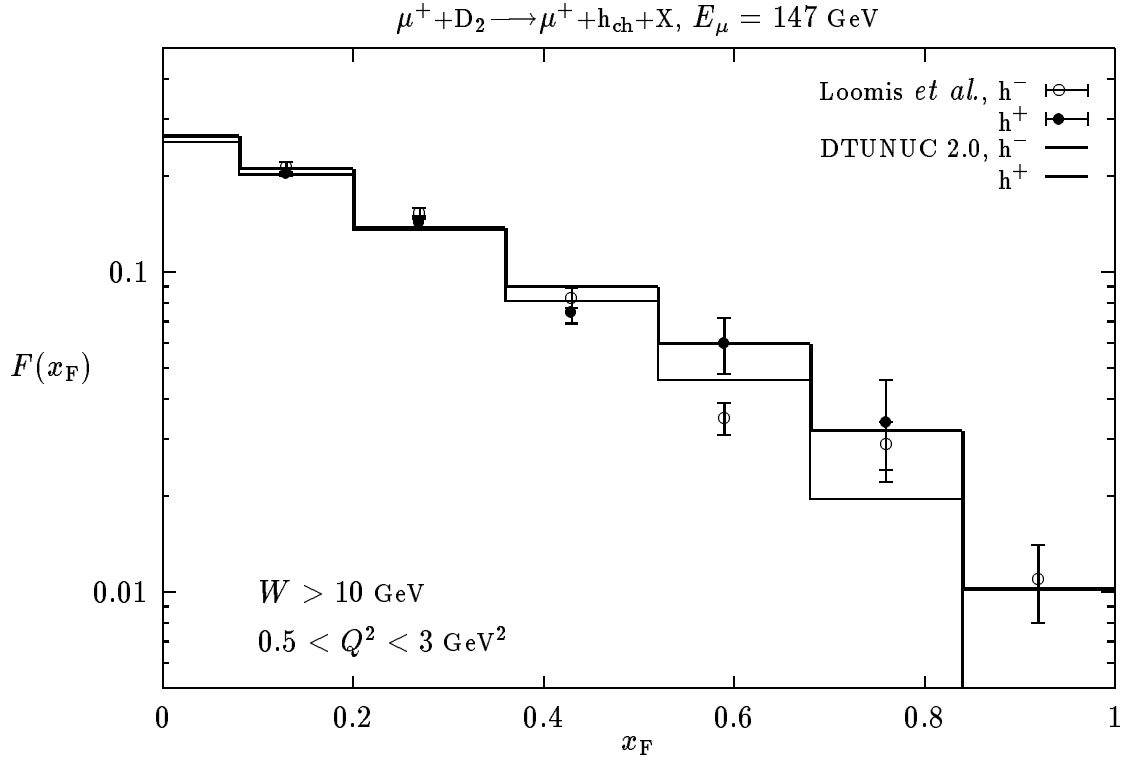
Fig. 10



a)



b)



c)

Fig. 11

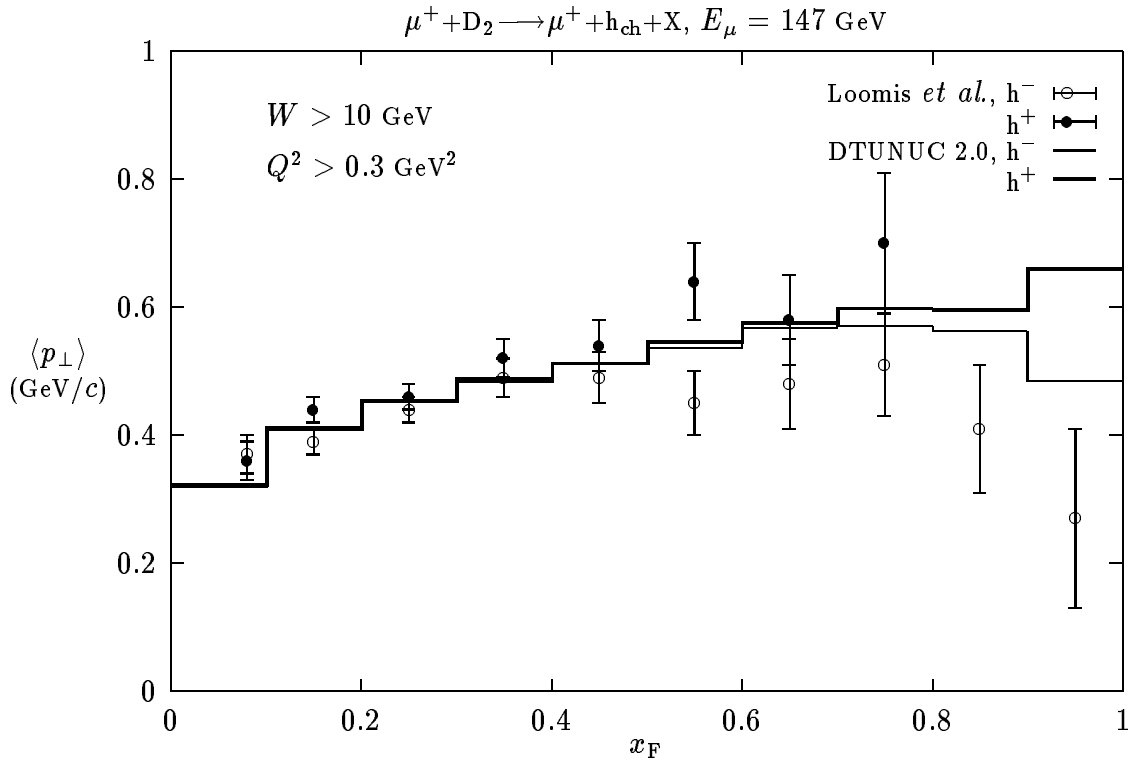
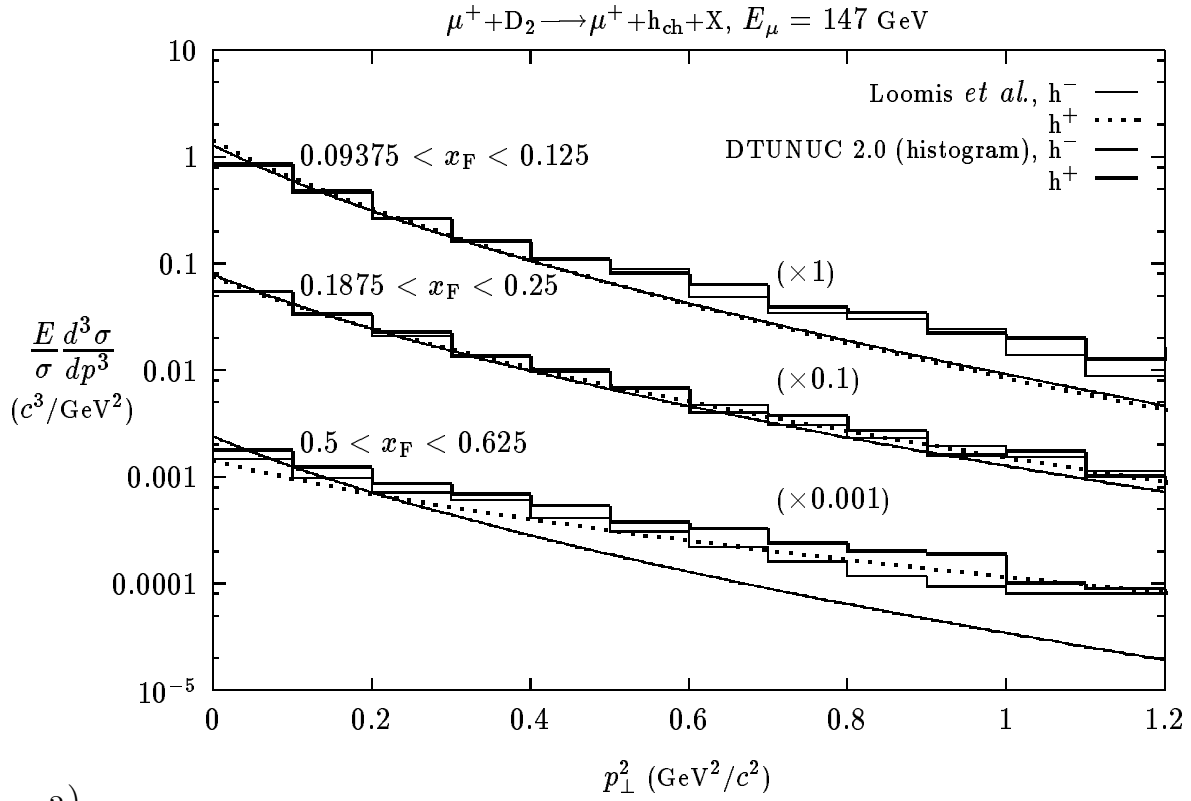
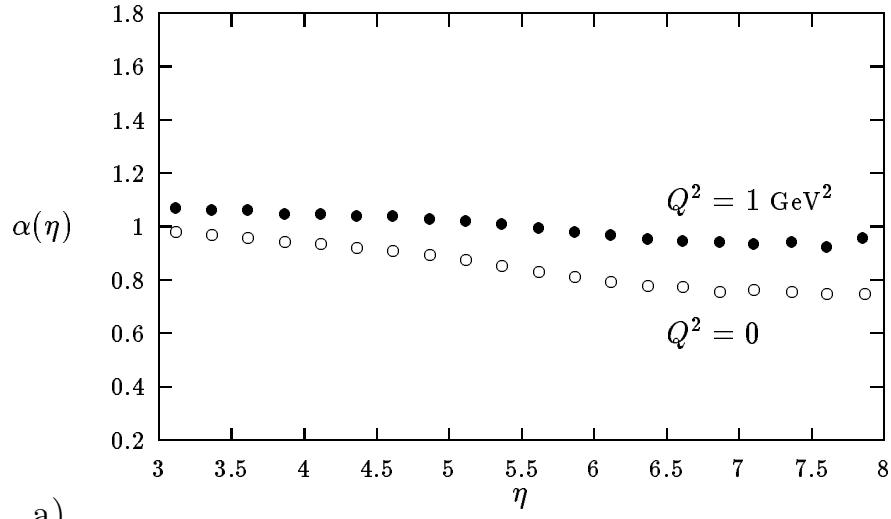
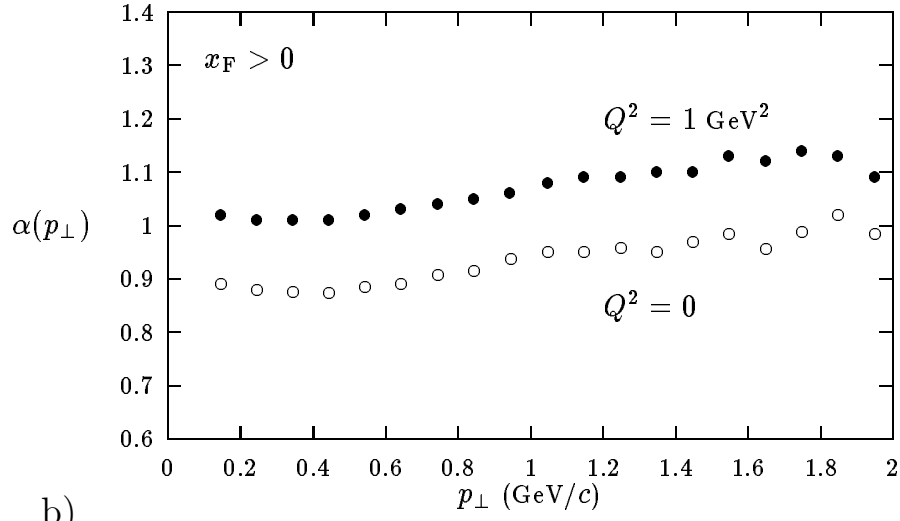


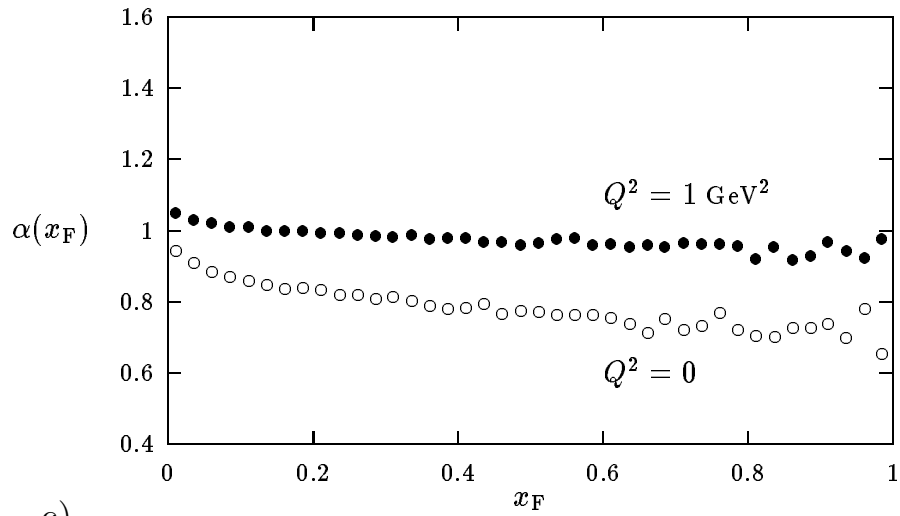
Fig. 12



a)



b)



c)

Fig. 13

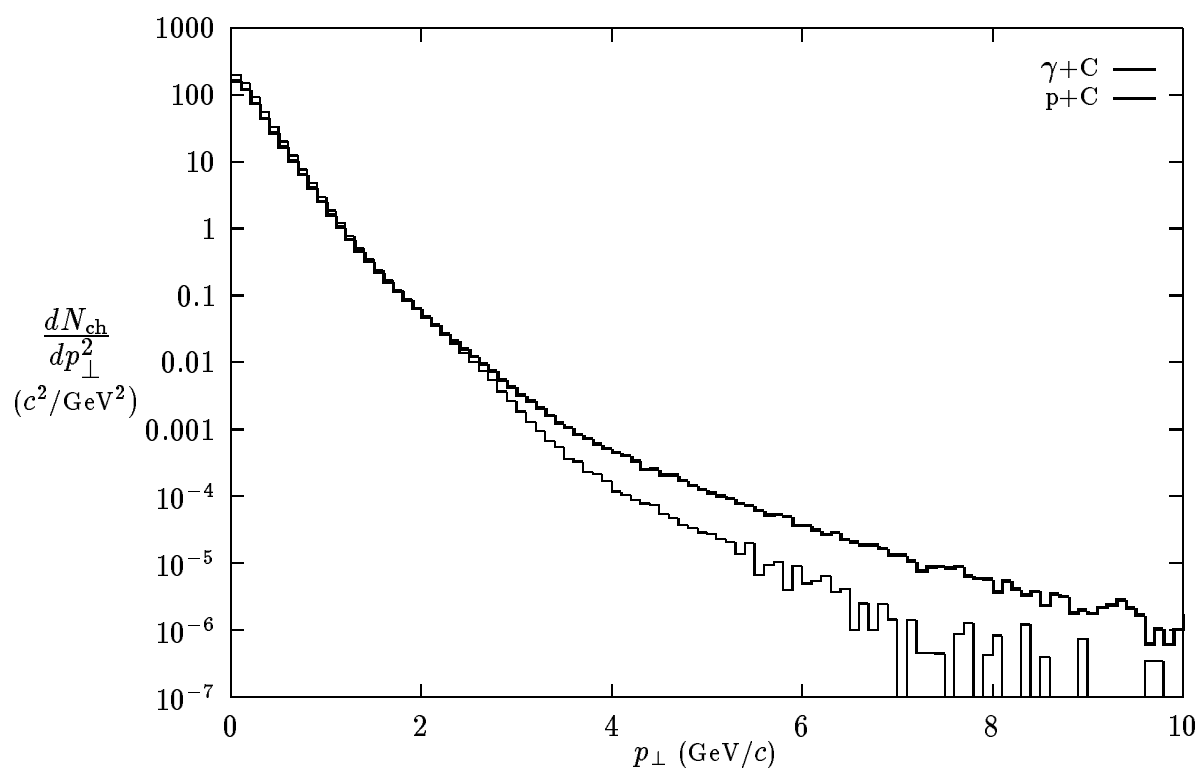
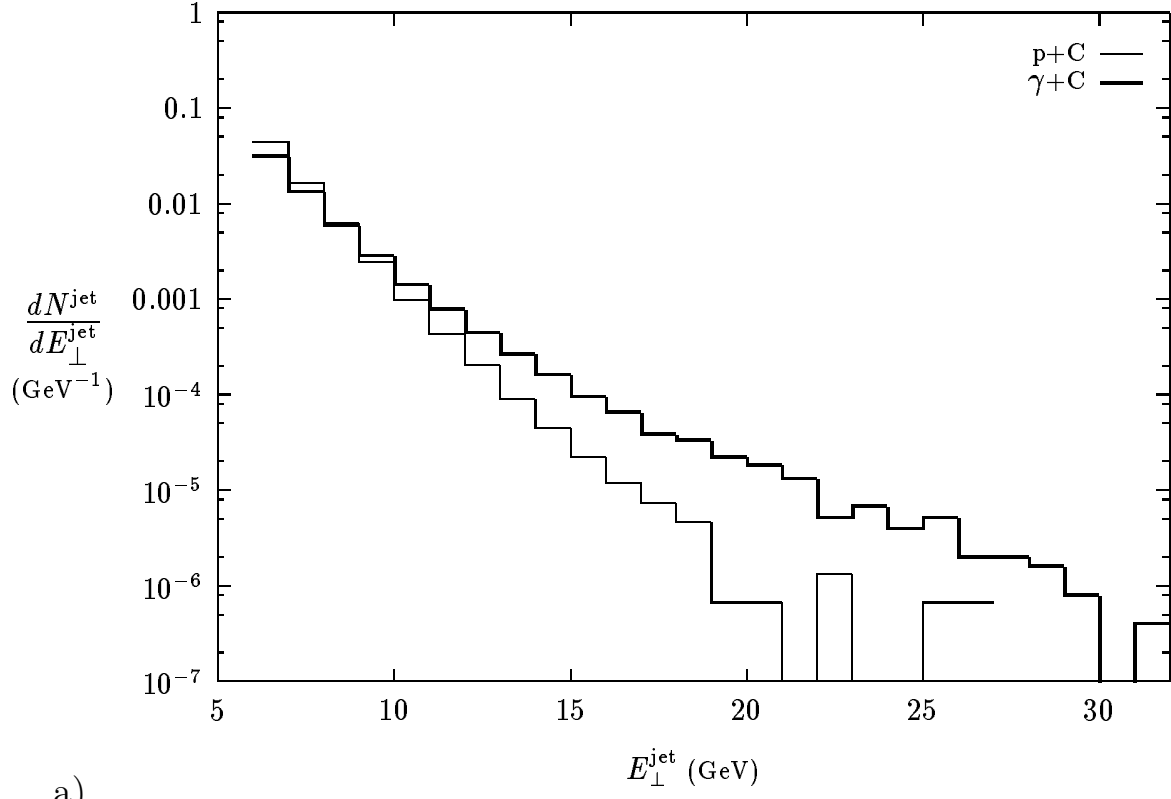
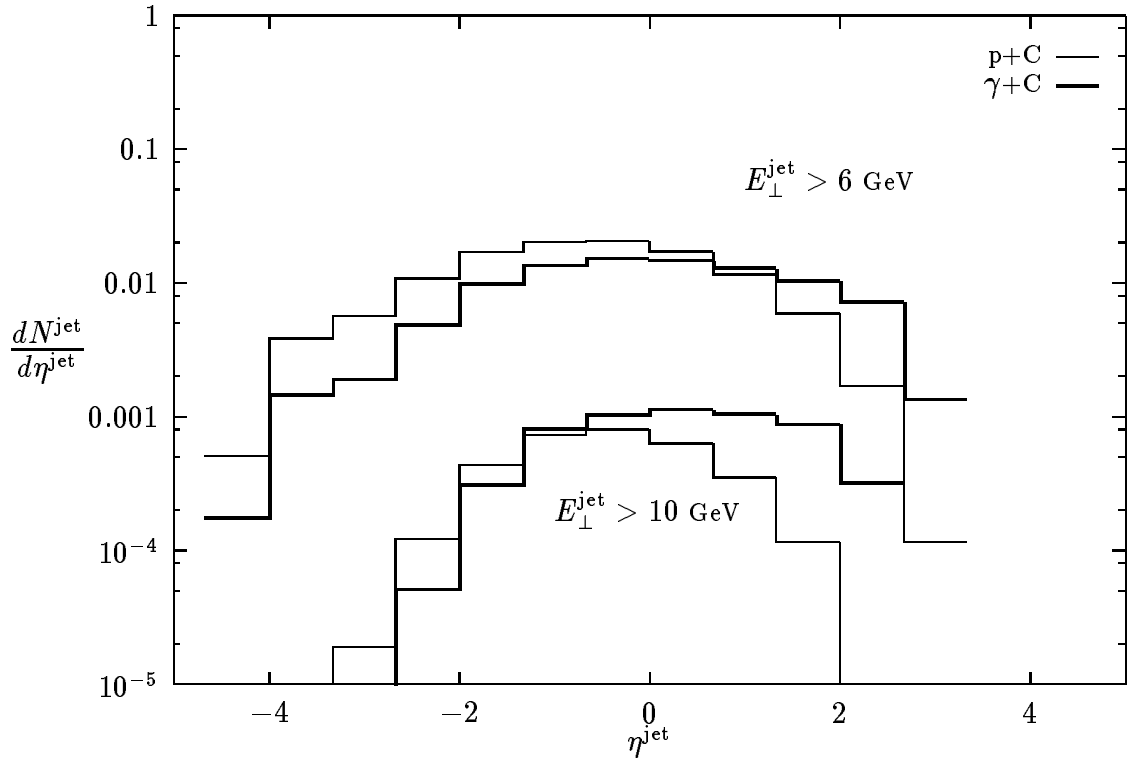


Fig. 14



a)



b)

Fig. 15

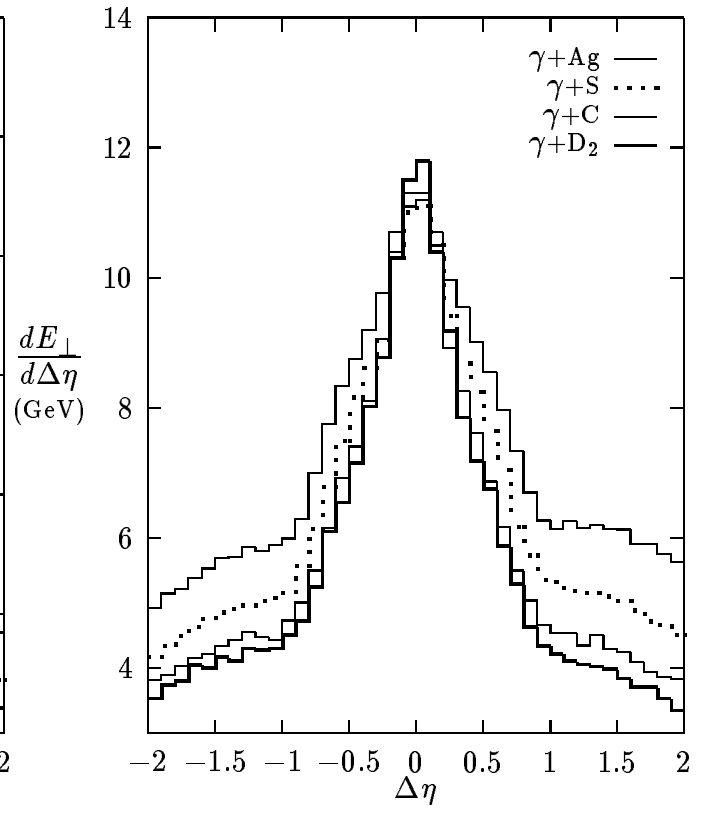
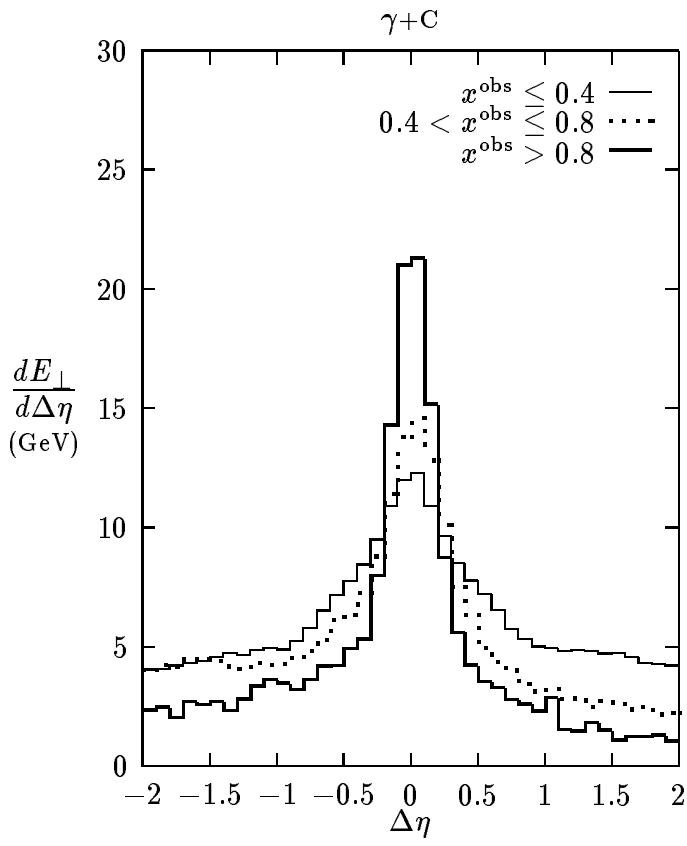
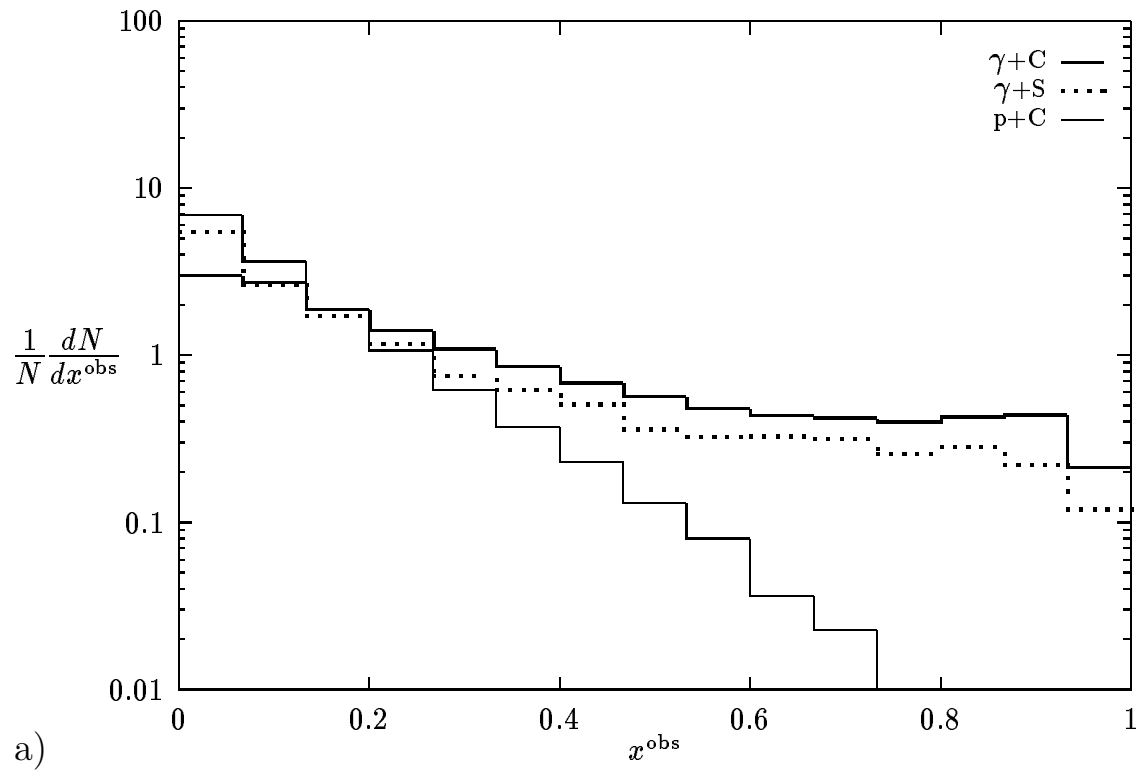


Fig. 16